

Article

# Mineralogy and Geochemistry of Mud Volcanic Ejecta: A New Look at Old Issues (A Case Study from the Bulganak Field, Northern Black Sea)

Ella Sokol<sup>1</sup>, Svetlana Kokh<sup>1,\*</sup>, Olga Kozmenko<sup>1</sup>, Sofya Novikova<sup>1</sup>, Pavel Khvorov<sup>2</sup>, Elena Nigmatulina<sup>1</sup>, Elena Belogub<sup>2</sup> and Maxim Kirillov<sup>1</sup>

<sup>1</sup> VS Sobolev Institute of Geology and Mineralogy Siberian Branch Russian Academy of Sciences, 3 Koptyug Avenue, Novosibirsk 630090, Russia; sokol@igm.nsc.ru or sokol\_ag@mail.ru (E.S.); olg@igm.nsc.ru or okozmenko@gmail.com (O.K.); sa\_novikova@inbox.ru (S.N.); helena@igm.nsc.ru (E.N.); kirillovm@igm.nsc.ru (M.K.)

<sup>2</sup> Institute of Mineralogy of the Urals Branch of the Russian Academy of Sciences, Miass 456317, Russia; khvorov@mineralogy.ru (P.K.); belogub@mineralogy.ru (E.B.)

\* Correspondence: s.n.kokh@gmail.com or zateeva@igm.nsc.ru; Tel.: +7-383-333-21-49

Received: 16 July 2018; Accepted: 6 August 2018; Published: 8 August 2018



**Abstract:** We characterise the mineralogy and geochemistry of Oligo-Miocene Maykopian shales that are currently extruded by onshore mud volcanoes of the Kerch-Taman Province (the Northern Black Sea) from the depths of ~2.5–3 km. The ejected muds are remarkable by highly diverse authigenic mineralogy that comprises glauconite, apatite, siderite, mixed Fe–Mg–Mn–(Ca) and Mn–Ca–Fe-carbonates, pyrite, marcasite, sphalerite, cinnabar, chalcopyrite, nukundamite, akantite, native Cu, Au and Au–Ag alloys. Precise geochemical techniques and high-resolution methods are applied to study the composition of bulk rocks, sulphide and carbonate fractions, as well as individual mineral species, including trace element and isotopic compositions of carbonates (C, O) and pyrite (S). Mineralogy of clastic and heavy fractions is used as a provenance tracer. Oxygen-deficient to weakly sulphuric deposition conditions are inferred for the parent sediments proceeding from trace element partitioning between carbonate, sulphide, and metallic phases. The main conclusion of the study is that onshore mud volcanoes of the region only transport buried sedimentary material and authigenic minerals they store to the ground surface.

**Keywords:** authigenic minerals; mud volcano; Maykop shale; Kerch-Taman Province; carbonate; sulphide; trace element partitioning; suboxic deposition conditions

## 1. Introduction

Mud volcanoes (MVs), which are actually “tectonic windows” into the deeper subsurface, have attracted the attention of geoscientists for at least 150 years [1–6]. The previous studies mainly address the morphology of volcanic edifices; the mechanisms, duration and periodicity of eruptions; the relations of mud volcanism with geological settings, overpressure zones, and oil and gas reservoirs; the geochemistry of MV fluids and mud (to a lesser extent), with implications for the compositions and depths of mobilised sediments; and the role of mud volcanism in the degassing of deeply buried sediments [2,7–17].

Meanwhile, the mineral-forming potential of mud volcanism has been less studied. Two most obvious types of mineral-forming processes are (1) surface and near-subsurface precipitation of salts (chlorides, borates, sulphates, and carbonates) from aqueous MV fluids on an evaporation barrier [3,18] and (2) ultra-high temperature alteration (combustion metamorphism) of mud masses triggered by MV flame eruptions and methane ignition [1,17,19–24]. In both cases, minerals owe their origin mainly

to fluids released through MV edifices. Crystal growth under these conditions commonly occurs as a disequilibrium process at abruptly changing pressure and temperature, which leaves imprint on the habits, compositions, and zonation of the solids.

For decades, the mineralogical study of ejected mud masses (MMs) has been mostly focused on applied issues related to petroleum exploration: identifying layered silicates as proxies of parent rock maturation degree and mobilisation depth [1,25–27] and heavy minerals as tracers of sediment provenance and diagenesis [26,28,29]. Detailed investigations into ongoing mineral-forming processes at offshore MVs and related methane seeps began in the 2000s and have shown that precipitation of minerals (mainly Ca-bearing carbonates) in mud may be mainly driven by methane emission and subsequent anaerobic oxidation [30–34]. According to the available knowledge, fluids appear to be the main mineral-forming agents in mud volcanic events.

We study mud masses (MMs) of ordinary onshore MVs of the Northern Black Sea region (the Bulganak field of the Kerch-Taman MV Province). This work, aiming at understanding the origin of diverse authigenic minerals stored in MMs, is a first step toward exhaustive characterisation of the onshore MV ejecta mineralogy. We have analysed more than twenty mineral species using the conventional tools and protocols of mineralogical research, and also checked numerous geochemical criteria discriminating between the mineral assemblages that formed syngenetically with the host mudrocks and later during mud volcanism.

The Bulganak mud volcanoes are the largest representative active onshore MVs of the region. They expulse aqueous fluids of a Cl-HCO<sub>3</sub>/Na type with low (SO<sub>4</sub>)<sup>2-</sup> contents and negligible amounts of H<sub>2</sub>S [3,18,35]. Having the deepest roots in the area (at least 2.5–3.5 km), these volcanoes bring to the surface material of a single type: homogeneous marine mudrocks of the Maykop Formation [3,18]. The Maykop monotonic Oligo-Miocene marine sequence has been quite well documented being a main source of MVs over the vast area from the Kerch Peninsula in the northern Black Sea region to the Cheleken Peninsula in the eastern Caspian coast [3,5,8,16,36–39].

We study mineralogy and geochemical signatures of bulk sediments and selected mineral fractions, as well as individual minerals (siderite, mixed Fe–Ca–Mg- and Mn–Ca–Fe-carbonates, pyrite, marcasite, sphalerite, cinnabar, Cu and Ag sulphides, metallic species and sulphates) and mineral generations (early framboidal and late euhedral pyrite), in order to track general patterns of trace element (TE) partitioning between coexisting minerals. The results are further used to reconstruct the origin of authigenic mineral assemblages, which potentially may (1) form by precipitation from (or interaction with) MV fluids or (2) be inherited from the parent Oligo-Miocene Maykop mudrocks, or (3) have a randomly combined (1) and (2) origin. There is a convincing proof that authigenic minerals store a detailed record of depositional environments and provide actual evidence of mineral formation conditions in diverse deposition settings [40–48]. Therefore, concordant changes in trace element and isotopic signatures of authigenic minerals coexisting in mud masses can provide a reliable check of their syngenetic origin.

## 2. Geological Context

### 2.1. Geological Setting and Paleoenvironments

The Black Sea basin is thought to be oceanic remnants now caught up in continental collision zones [49]. The Kerch and Taman Peninsulas separated by the narrow Kerch Strait lie in a geodynamically unstable area, at the junction of three regional-scale tectonic structures: the Highland Crimea and Greater Caucasus, the Indol-Kuban Trough, and the Kerch-Taman [3,50]. The Indol-Kuban Trough is a large sedimentary basin extending over 500 km from the Caucasus foothills in the east, through the Taman Peninsula, as far as the Kerch Peninsula in the west (Figure 1a). The sea basin currently undergoes enhanced lateral tectonic shortening, with mud volcanoes known at the front and in the centre of the accretionary wedge [2] (Figure 1a). Efficient dewatering during diagenetic dehydration reactions (smectite-to-illite conversion), organic matter maturation, and coupled oil and gas production in the

frontal and upper parts of the deforming wedge maintained generation of fluids and thus created undercompaction of sediments, overpressure and buoyancy as prerequisites for mud volcanism [2].

The Kerch-Taman MV Province is located on the southern periphery of the Indol-Kuban Trough where it is associated with thick Paleocene–Quaternary sediments that reach a total thickness of 11 km, including 2500–4000 m of Oligocene–Early Miocene (29–19 Ma) homogeneous clayey marine sediments known as the Maykop Formation or Maykop Shale. They are source and parent rocks to the MVs of the vast region and, at the same time, reservoir rocks that store significant resources of oil and gas in the Taman Peninsula and in the basins bordering the Greater Caucasus [3,5,36,37,51–55].

The Maykop Formation was deposited in the time of dramatic palaeogeographic changes in the eastern part of the former Tethys ocean induced by the African/Arabian–Eurasian continental collision since the Eocene [51]. The collision led to uplift of the Alpine chain and to break-up of the Tethyan Realm into the southern (circum-Mediterranean) and northern (Paratethyan) domains. From the Oligocene onward, the northern domain became subject to recurrent isolation from the Mediterranean [54,55]. The postcollisional isolation of the inland Paratethyan basin, along with a moderately warm and humid climate, resulted in an estuarine water circulation pattern and halocline formation, which caused recurrent stagnancy in the water column. Those events were accompanied by sealevel rise and transgression onto a vast area of the southern Russian Platform. Thus, the Russian landmass in the north and the Lesser Caucasus–Elburz–Kopet–Dag ranges in the south were main sources of clastic inputs into that part of the Eastern Paratethys basin. Clastics were transported to the western Indol-Kuban Trough mainly from the Ukrainian and Donets provenance areas and were deposited as the Maykop suboxic shales without age-diagnostic fossils [3,50,52,54,55]. In the Middle Miocene, the southern side of the Indol-Kuban Trough underwent folding and thrusting, with clay diapirism and mud volcanism at the front. Mud volcanism in the Kerch-Taman Province culminated in the Middle–Late Miocene but is currently declining [3]. Altogether there are nineteen and fifteen MV fields associated with Maykop Shales in the Kerch and Taman Peninsulas, respectively. All active MV domes are located in the axial onshore part of the overpressure zone. Offshore mud volcanism occurs in the southern Sea of Azov and in the northern continental slope of the Black Sea [3,56–58].

## 2.2. The Kerch Peninsula: Local Geology and Maykopian Facies

The study area is located in the northwestern Kerch Peninsula, on the southern side of the Indol-Kuban Trough (Figure 1) [51,53,59]. The present tectonic framework of the area comprises numerous small W–E folds with curved axes (Figure 1b). There are four W–E anticlinal zones composed mainly of Neogene sediments [3,50]. Folding in the Kerch Peninsula was often accompanied by clay diapirism and extrusion of plastic mud by active and fossil mud volcanoes clustering in cores of large anticlines. The Kerch mud volcanoes are currently undergoing a gryphon–salsa activity phase, with moderate gas emanation and expulsion of mud and saline waters. Their features have been exhaustively covered by previous workers [3,18,59–61] and will be left beyond this consideration.

The Lower and Middle Maykop sediments are ubiquitous in the Kerch Peninsula but are rarely exposed, being most often buried under mudrocks and recent alluvial and aeolian deposits. The Middle Maykop section, varying in thickness from hundreds of meters in the southern part of the peninsula to 1000–2500 m in the north, comprises a clay unit below and a sand-clay unit above. In the east and northeast, it consists of mostly homogeneous deep-sea mudrocks depleted in both carbonates and organic matter [62]. The total thickness of the Maykop Formation within this area approaches its regional maximum of 3700–4200 m. Drilling in the Bulganak MV field revealed Middle Maykop sediments at a depth of 2000 m and more [3]. The Upper Maykop rocks are widespread in the Southwestern Plain of the Kerch Peninsula and locally fill synclines in its north–east [3]. Thin layers of the Maykop Formation crop out locally in cliffs on the southern Azov Sea coast. The outcrop nearest to the Bulganak MV field is that of the Upper Maykop unit, with typical siderite lenses and layers, at the Tarkhan Cape (10 km away), while the nearest bedrock exposure of monotonous mudrocks that belong to this unit is as far as in the Taman Peninsula (Kamennyi Cape, 50 km away). Both outcrops

expose only thin intervals (15 and 5–7 m, respectively), which we sampled and studied together with the currently extruded mud mussels.

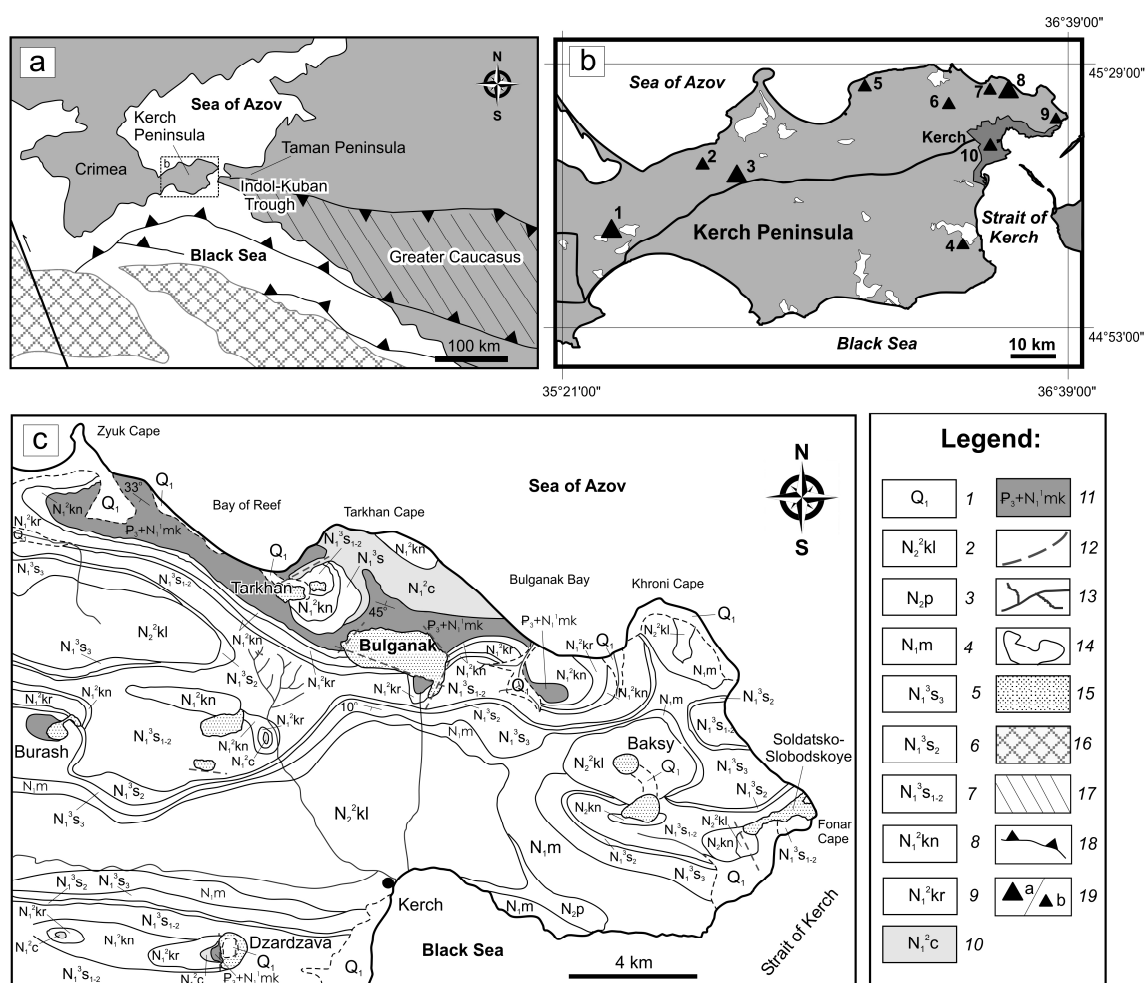


**Figure 1.** (a) Sketch map of the northeastern Black Sea region. Modified after [2]; (b) Location map of sampled mud volcanoes in the Kerch-Taman MV province. Modified after [3]. Grey colour—onshore area; white colour—offshore area. Mud volcanoes: Vladislavovskiy (1), Nasyr (2), Korolevskiy (3), Tobichek (4), Suyurtash (5), Burash (6), Big Tarkhan (7), Bulganak field (8), Eny-Kale (9), Soldatsko-Slobodskoye (10); (c) Detailed geological map showing locations of mud volcanoes, geological structures and their sedimentary stratigraphy in the northeastern Kerch Peninsula. Modified after [59]. 1—Lower Quaternary sand, clay silt, and clay ( $Q_1$ ); 2—Middle Pliocene sand, clay, and iron ore (Kuyalnik stage  $N_2^2kl$ ); 3—Lower Pliocene (Pontic stage  $N_2p$ ) shelly limestone, and clay; 4—Upper Miocene shelly limestone, reefal limestone with bryozoa, and clay (Meotic stage  $N_1m$ ); 5—Upper Miocene clay, marl, and limestone (Sarmat stage, upper substage  $N_1^3s_3$ ); 6—Upper Miocene clay, marl, limestone, and sand (Sarmat stage, middle substage  $N_1^3s_2$ ); 7—Upper Miocene clay with sand, marl, and shelly limestone interbeds (Sarmat stage, lower and middle substage  $N_1^3s_{1-2}$ ); 8—Middle Miocene organic limestone, gypsum, and clay with marl and sand interbeds (Konk stage  $N_1^2kn$ ); 9—Middle Miocene organic limestone, gypsum, and clay with marl and sand interbeds (Karagan stage  $N_1^2kr$ ); 10—Middle Miocene organic limestone, gypsum, and clay with marl and sand interbeds (Chokrak stage  $N_1^2c$ ); limestone aquifers; 11—Oligocene and Lower Miocene shale and silt (Maykop Formation  $P_3 + N_1^1mk$ ); 12—faults, 13—rivers, 14—stratigraphic boundaries; 15—mud volcanic field; 16—oceanic crust; 17—Alpine orogens; 18—Post-Eocene thrust; 19—a—large MV domes, b—small MV edifices.

### 2.3. Study Area

The northernmost zone of anticlinal folds (Chegene-Yenikale) lies in the extreme northeast of the Kerch Peninsula, near the Azov coast, where the largest Bulganak field of mud volcanoes (Figures 1b and 2) is located in the depression of the same name, 8 km north of Kerch city. The field occurs on the eroded crest of the Bulganak anticline which has Middle Maykop shales in its core [3]. Several bowl-shaped depressions in the anticline crest are surrounded by nine flat mud volcanic edifices, gryphons, salsas, and mud lakes (Figures 2 and 3). We chose to sample MMs from three representative mud volcanoes (Andrusov, Trubetskoy, and Tischenko Hills) in the Bulganak field for detailed mineralogical analyses (Figures 2 and 3).

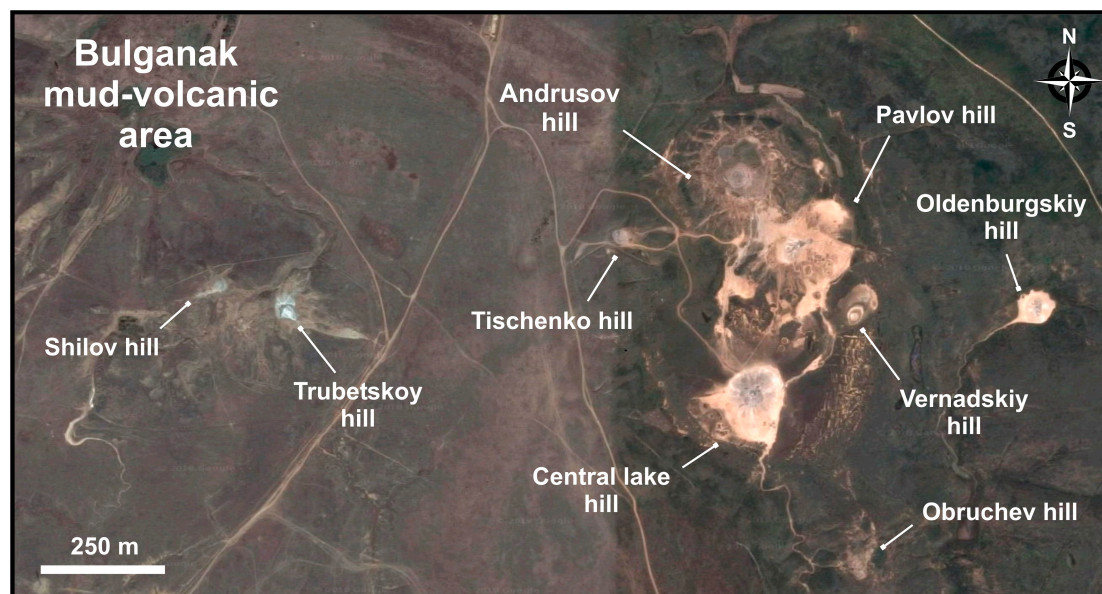


**Figure 2.** Study area. Panoramic view of the Bulganak field of mud volcanism. Google Earth image, 2007.

The Bulganak mud volcanoes extrude solid material from deep parts of the Middle Maykop section, as it was reconstructed proceeding from the geological setting, drilling data, composition of mud masses [3], micro-palaeontological data [24], and estimates of fluid generation temperatures [18,59]. Earlier results show that waters released by different Kerch MVs are similar to pore waters in the Middle Maykop strata [3,18,24,35,61,63,64]. The MV waters have pH = 7.0–8.7, normally contain 10 to 18 g/L total dissolved solids (TDS) (up to 69.0 g/L), and belong to Cl-HCO<sub>3</sub>/Na or more rarely to HCO<sub>3</sub>-Cl/Na types with low Ca, Mg concentrations and (SO<sub>4</sub>)<sup>2-</sup> contents from 0 to 110 mg/L. Compared with seawater (SW), they exhibit profound freshening for Na, K, Rb, Ca, Mg, Sr, (SO<sub>4</sub>)<sup>2-</sup>, Cl, and Br (MV water/SW ratios 0.01–0.7), but strong enrichment in mobile B, Li, Ba, P, and As. The highest trace element concentrations were measured in the Bulganak gryphon and salsa waters (B—305–1635 ppml; Li—1.5–8.2 ppml) [18]. Abundant current precipitates growing from the MV waters of the area are chiefly Na–Ca and Na borates (ulexite NaCa(B<sub>5</sub>O<sub>6</sub>(OH)<sub>6</sub>)·5H<sub>2</sub>O; probertite NaCa(B<sub>5</sub>O<sub>7</sub>(OH)<sub>4</sub>)·3H<sub>2</sub>O; borax Na<sub>2</sub>(B<sub>4</sub>O<sub>5</sub>(OH)<sub>4</sub>)·8(H<sub>2</sub>O); tinalconite Na<sub>6</sub>(B<sub>12</sub>O<sub>15</sub>(OH)<sub>12</sub>)·8H<sub>2</sub>O) with lesser amounts of Na-bearing carbonates (gaylussite Na<sub>2</sub>Ca(CO<sub>3</sub>)<sub>2</sub>·5H<sub>2</sub>O and northupite Na<sub>3</sub>Mg(CO<sub>3</sub>)<sub>2</sub>Cl), and sporadic CaCO<sub>3</sub> [18], unlike the calcite-dominated active and dormant travertine springs from the adjacent Big Tarkhan locality [59].

The generation temperatures of aqueous fluids released from the Bulganak MVs, estimated using the chemical Mg/Li geothermometer (T<sub>Mg/Li</sub>) [65], fall within the T<sub>Mg/Li</sub> range from 76 to 117 °C (n = 14). The respective depths (H<sub>Mg/Li</sub>) of mud volcanic roots, as inferred from these temperatures and measured local geothermal gradients (30–35 °C/km) [66,67], vary from 2.5 to 3.5 km. The T<sub>Mg/Li</sub> range for the Big Tarkhan travertine springs is 68–78 °C, which corresponds to a depth of 2.0–2.5 km [59].

Compared with the Big Tarkhan and Taman MVs [64,68], those from the Bulganak field expulse fluids from greater depths.

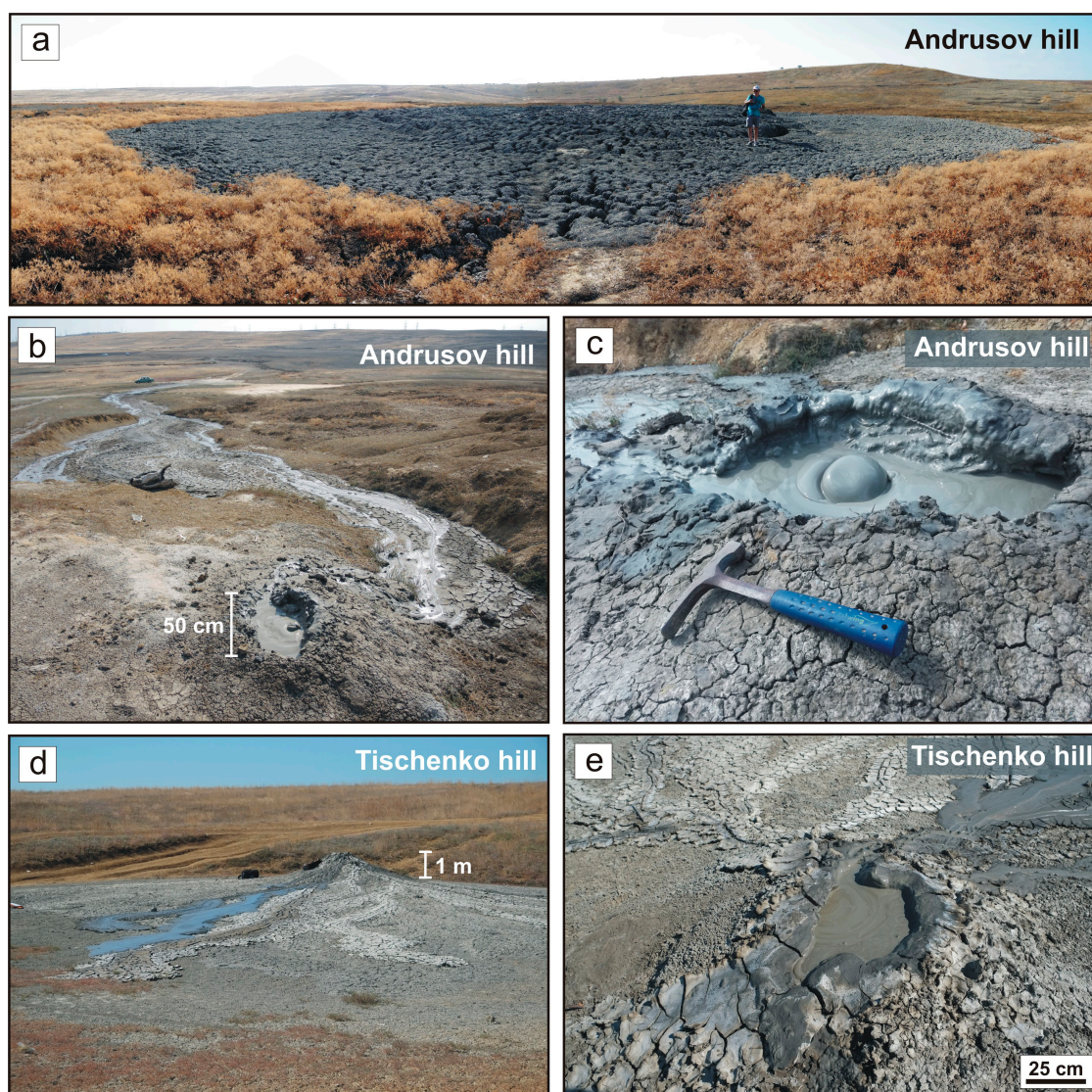


**Figure 3.** Field view of the Bulganak MV field (September 2017). (a) Main eruptive center of Andrusov Hill extruding plastic mud masses. (b,c) A bubbling satellite gryphon on the flank of the main cone (Andrusov Hill). (d) Panoramic view of Tischenko Hill expulsing liquid mud. (e) Bubbling craters at the top of Tischenko Hill.

### 3. Materials and Methods

#### 3.1. Sampling

In the course of 2008–2017 field trips, we collected bulk samples of Upper and Middle Maykop shales from the coastal cliffs, along with fifty samples of liquefied Middle Maykop shales as currently extruded fresh and slightly weathered mud masses (MMs) from ten mud volcanoes in the Kerch Peninsula. Eleven large (120 kg) bulk MM samples were taken from edifices in the Bulganak field for most detailed mineralogical analyses. In the first step, clay and heavy minerals (HM) and carbonate fractions ( $\leq 1$  mm) were extracted from the bulk samples and subjected to several procedures of gravity and electromagnetic separation. They were layered silicates ( $< 2 \mu\text{m}$ ) (1), concentrates of sulphides (2), Fe-rich carbonates (3), a fraction of Fe-(oxy)hydroxides (4), stable HM from the clastic fraction (5), light

fraction (6) with predominant quartz sand particles and sporadic fossil remnants consisting mainly of  $\text{CaCO}_3$ . Then pyrite (framboids and euhedral crystals separately), marcasite and carbonate fractions were hand-picked under a binocular microscope. Only optically clean grains without visible impurities were selected for the chemical and isotope analyses.

### 3.2. Analytical Procedures

Most of the analytical procedures were carried out at the Analytical Center for multi-elemental and isotope research (VS Sobolev Institute of Geology and Mineralogy, Novosibirsk, Russia). Sulphur isotopic compositions of pyrite and X-ray analyses of bulk sediments were carried out at the Institute of Mineralogy (Miass, Russia). Laser ablation-inductively coupled plasma-mass spectrometry (LA-ICPMS) of  $\text{FeS}_2$  was performed at the Centre for Ore Deposit and Exploration Science (CODES), University of Tasmania.

The elemental compositions of the Maykop Shale bulk samples and isolated mineral fractions were studied by the solution analysis using inductively coupled plasma atomic emission spectroscopy (ICP-AES) and inductively coupled plasma mass spectrometry (ICP-MS). The preconditioning procedures included fusion of powdered whole rock samples with lithium borate following Shatsky et al. [69]; purifying sulphide fractions by 2 wt % HCl with subsequent rinsing in MQ-water; and digestion of carbonate and purified sulphide fractions in fresh aqua regia. Thus, obtained solutions were divided into two aliquots for analyses of major and trace elements. The aliquots for trace element analysis were diluted with 2 wt %  $\text{HNO}_3$ . Major elements (Si, Ti, Al, Fe, Mg, Ca, Na, K, P, S) were analysed on a *IRIS Advantage atomic emission spectrometer* (ThermoJarrell Intertechs Corporation, Atkinson, WI, USA). Scandium was added as an internal standard to correct matrix effects and instrument drift. The concentrations of trace elements (V, Cr, Mn, Co, Ni, Cu, Zn, Ga, As, Rb, Sr, Zr, Nb, Mo, Ag, Cd, Sb, Te, Cs, Ba, Hf, Au, Ta, Tl, Pb, Bi, Th, U, and REE + Y) were determined on an *ELEMENT ICP-MS* (Finnigan, Waltham, MA, USA), using indium as an internal standard for correction of matrix effects and instrument drift. The detection limits for trace elements were in the range 0.01–0.2  $\mu\text{g/L}$ . Precision and accuracy for all elements were estimated to be 5–10 rel %. Two standards (BCR-2, BHVO-2) were used for monitoring analytical reproducibility.

Hg contents in the bulk samples of sediment and in pyrite and marcasite concentrates were measured by flameless AAS on a Hg analyser *RA-915M* (Lumex, Saint-Petersburg, Russia) with a RP91C pyrolysis attachment. The technical specifications of the instruments allow avoiding special preconditioning of solid samples. The standard SDPS-3 was used to calibrate the spectrometer. Relative analytical errors were less than 20% ( $p = 0.95$ ) for concentrations from  $5 \times 10^{-7}$  to  $2.5 \times 10^{-2}$  wt % [70].

Scanning electron microscopy (SEM) and energy dispersive X-ray spectroscopy (EDS) were applied to several tens of mineral grains and aggregates to determine features of their textures, morphology, and mineral chemistry. The analyses were performed on a *JSM-6380LA* scanning electron microscope (JEOL Ltd., Tokyo, Japan) at an accelerating voltage of 10 kV and a beam current of 2.0 nA. The chemical compositions of carbonate and sulphide grains were determined by wavelength-dispersive electron microprobe analysis (EMPA) in carbon-coated polished samples, using a *JXA 8100* electron microprobe (JEOL Ltd., Tokyo, Japan). EMPA analyses of carbonates were performed using an accelerating voltage of 20 keV, a beam current of 15 nA, a 10 s peak counting time, and a 3–5  $\mu\text{m}$  beam diameter. The compositions of carbonates were estimated with reference to natural and synthetic standards: albite (Na), diopside (Mg, Ca),  $\text{BaSO}_4$  (Ba), pyrope (Fe), Sr–Si glass (Sr), Mn-almandine (Mn),  $\text{ZnFe}_2\text{O}_4$  (Zn) [71]. The concentrations of impurities in sulphides were estimated under the operating conditions of 20 keV accelerating voltage, 50 nA beam current, 20 s total counting time, and a focused incident beam. The standards included  $\text{FeS}_2$  (S, Fe),  $\text{FeAsS}$  (As),  $\text{PbTe}$  (Pb),  $\text{FeNiCo}$  (Co, Ni), Sb-metal (Sb), Mn-almandine (Mn), ZnS (Zn),  $\text{CuFeS}_2$  (Cu), CdS (Cd) and HgS (Hg). The detection limits for the elements were (in wt %): 0.01 for Fe, Mn, As, Cu, and Ni; 0.02 for S and Co; 0.03 for Zn; 0.04 for Sb; 0.05 for Hg; and 0.07 for Cd. Peak overlaps for  $\text{CaK}_\beta$ - $\text{PK}_\alpha$  and  $\text{SiK}_\alpha$ - $\text{SrL}_\alpha$  were automatically compensated by the instrument software; the matrix correction

using the ZAF algorithm [72] was applied to raw data prior to recalculation into major oxides or elements. The analytical accuracy was better than 2 rel % for >5 wt % elements and about 5 rel % for  $\leq 2$  wt % elements.

Trace element abundances in FeS<sub>2</sub> were determined by the LA-ICPMS technique at the School of Earth Sciences, University of Tasmania and Centre for Ore Deposit Research (Hobart, Australia). The analyses were performed on a quadrupole 7900cs mass spectrometer (Agilent, Santa Clara, CA, USA) and a 193-nm wavelength COMPex Pro ArF gas laser (Coherent Inc., Santa Clara, CA, USA) with resonetics constant geometry design produced by the Laurin ablation cell. Each sample was analysed in a time-resolved mode using (Table S1) ms integration time, 1 point per mass, and 60 s total acquisition time, with approximately 20–25 s of data collected on the gas background prior to ablation. Most analyses used a 30- $\mu$ m spot diameter with a laser repetition rate of 5Hz and a power set to  $\sim 6.5$  mJ/pulse. All analyses were normalised to external standards (STDGL3 and GSD-1G) and to a reference element (Fe) as an internal standard. Analytical errors for most elements were less than 5% (Table S1), which is the typical precision of LA-ICPMS systems in the multi-element mode.

X-ray diffraction (XRD) analyses of phases in the MMs, Maykop shale bulk samples and selected fractions were performed on a XRD-6000 diffractometer (Shimadzu Corporation, Kyoto, Japan) (CuK <sub>$\alpha$ 1+2</sub> radiation with graphite monochromator), at 4° to 70° 2 $\theta$ , at a step of 0.5°. Layered silicates were extracted following the method of Hubert et al. [73] in a <2  $\mu$ m fraction obtained by a sedimentation technique using repeated siphoning. According to the recommendations for exact identification of layered silicates [74], <2  $\mu$ m fractions were reanalysed after being saturated in glycerol for 24 h and heated at 550 °C for 1 h. SIROQUANT V.4 software was used to calculation of the proportions of minerals.

For measurements of C and O stable isotopes, powdered carbonate fractions were dissolved in 100% phosphoric acid at 50 °C for over 48 h and then analysed on a Gas Bench II instrument coupled with a MAT 253 mass spectrometer (Thermo Finnigan, Waltham, MA, USA). All isotope values are quoted per mill (‰) using  $\delta$ -notation relative to the Vienna-PeeDee Belemnite standard (VPDB), with a standard deviation of less than 0.1‰ for  $\delta^{13}\text{C}$  and 0.2‰ for  $\delta^{18}\text{O}$ . Sulphur isotopic compositions of pyrite (quoted as  $\delta^{34}\text{S}$  per mil relative to the Canyon Diablo Troilite (CDT) standard) were analysed on a Delta+ Advantage mass-spectrometer (Thermo Finnigan, Waltham, MA, USA) using NBS-123 and IAEA-S-1 standards, with  $\delta^{34}\text{S}$  values reproduced to no worse than 0.15‰ CDT.

## 4. Results

### 4.1. Bulk and Trace Element Chemistry of the MMs

Mud masses consist of the liquefied Middle Maykop shale with a moderate amount of sand and low organic contents ( $\leq 0.5$  wt %). All MMs are depleted in K (0.7–0.8) relative to Post-Archean Australian Shale (PAAS) [75] (Tables 1 and 2; Figure 4), which is due to high percentages (up to 25–30%) of kaolinite among layered silicates (mainly illite and interlayered illite-smectite) (Figure 5). Variable amounts of authigenic and biogenic carbonates, as well as the presence of chemogenic celestine and barito-celestine, are responsible for variations in Ca and Sr contents. Unlike weathered MMs, the fresh samples contain more sulphidic than sulphate sulphur and more Fe<sup>2+</sup> than Fe<sup>3+</sup>. The MMs are commonly enriched in Na and B relative to PAAS and Li, Cs, U, Zn, Co, V, As, Se, Sb, Hg, Cd relative to the average upper crust [76] (Figure 4). Excess sodium is mainly present as high-silica plagioclase of the sand fraction with minor NaCl, while boron mainly resides in Na–Ca and Na borates [3,18]. The MM samples enriched in Hg and As contain cinnabar and As framboidal pyrite.

Total rare-earth element (REE) contents in the Maykop Shales and MMs are 0.65 of PAAS (110–124 ppml against 184 ppml) (Table 2), but the PAAS-normalised REE patterns of the samples are similar to one another and to those of PAAS, being different only in more depleted light rare-earth elements (LREE) relative to heavy rare earths (HREE), with (LREE/HREE)<sub>SN</sub> = 0.70–0.75. Their

depletion in LREE, as well as in Cs, Rb, Pb, Th, U, Zr, Hf, Nb, and Ta records “dilution” with quartz, and kaolinite.

**Table 1.** Major element composition (in wt %) of representative mud masses from the Bulganak mud volcano area in comparison with Middle and Upper Maykop shales (Kerch-Taman MV province).

| Rocks                          | Middle | Upper   | Fresh Mud Masses |       |       |                  |      | Weathered Mud Masses |        |       |                  |      |
|--------------------------------|--------|---------|------------------|-------|-------|------------------|------|----------------------|--------|-------|------------------|------|
|                                | Maykop | Maykop  |                  |       |       |                  |      |                      |        |       |                  |      |
| Sample                         | T-1-3  | BT-18-1 | B-3-4            | O-1-2 | 202-2 | Mean<br>(n = 10) | S    | B-3-7                | 203-1s | 203-2 | Mean<br>(n = 11) | S    |
| SiO <sub>2</sub>               | 53.19  | 60.04   | 56.61            | 60.36 | 57.31 | 57.63            | 1.88 | 57.30                | 53.93  | 58.32 | 56.69            | 3.96 |
| TiO <sub>2</sub>               | 0.81   | 1.05    | 0.78             | 0.88  | 0.89  | 0.85             | 0.05 | 0.87                 | 0.82   | 0.85  | 0.85             | 0.04 |
| Al <sub>2</sub> O <sub>3</sub> | 16.48  | 18.07   | 14.19            | 12.73 | 12.70 | 13.87            | 1.50 | 15.81                | 14.82  | 14.23 | 14.47            | 0.99 |
| Fe <sub>2</sub> O <sub>3</sub> | 7.90 * | 5.83 *  | 1.57             | 2.06  | 2.19  | 2.16             | 0.52 | 5.18                 | 3.84   | 5.32  | 4.80             | 0.61 |
| FeO                            | n.a.   | n.a.    | 4.38             | 4.18  | 4.77  | 4.45             | 0.25 | 2.01                 | 2.83   | 1.55  | 1.84             | 0.70 |
| MnO                            | 0.11   | 0.04    | 0.07             | 0.10  | 0.10  | 0.09             | 0.01 | 0.08                 | 0.08   | 0.11  | 0.09             | 0.01 |
| MgO                            | 3.38   | 1.95    | 2.02             | 1.77  | 1.93  | 1.92             | 0.10 | 2.20                 | 1.89   | 1.93  | 1.89             | 0.28 |
| CaO                            | 2.44   | 0.47    | 1.82             | 1.84  | 2.15  | 1.81             | 0.29 | 1.40                 | 1.41   | 2.26  | 1.59             | 0.53 |
| Na <sub>2</sub> O              | 1.32   | 1.37    | 3.08             | 2.73  | 2.93  | 2.67             | 0.51 | 1.87                 | 3.98   | 1.97  | 2.90             | 1.64 |
| K <sub>2</sub> O               | 2.87   | 2.19    | 2.16             | 1.90  | 1.97  | 2.09             | 0.19 | 2.38                 | 2.25   | 1.98  | 2.14             | 0.21 |
| P <sub>2</sub> O <sub>5</sub>  | 0.11   | 0.10    | 0.14             | 0.14  | 0.13  | 0.14             | 0.01 | 0.13                 | 0.14   | 0.17  | 0.14             | 0.02 |
| H <sub>2</sub> O <sup>-</sup>  | n.a.   | n.a.    | 1.57             | 1.24  | 1.43  | 1.53             | 0.27 | 1.86                 | 1.84   | 1.99  | 2.16             | 0.60 |
| LOI                            | 9.98   | 7.84    | 7.07             | 5.68  | 6.16  | 6.42             | 0.62 | 6.71                 | 7.64   | 6.17  | 7.44             | 1.31 |
| CO <sub>2</sub>                | n.a.   | n.a.    | 3.99             | 3.71  | 4.82  | 3.93             | 0.67 | 2.17                 | 3.27   | 2.24  | 2.45             | 1.28 |
| F                              | n.a.   | n.a.    | 0.06             | 0.06  | 0.06  | 0.06             | 0.00 | 0.06                 | 0.06   | 0.05  | 0.06             | 0.01 |
| SO <sub>3</sub>                | 0.47   | 0.14    | 0.07             | n.d.  | 0.07  | 0.03             | 0.04 | n.d.                 | 0.93   | 0.25  | 0.24             | 0.40 |
| S                              | n.a.   | n.a.    | n.d.             | 0.27  | 0.15  | 0.17             | 0.12 | 0.10                 | 0.13   | 0.12  | 0.07             | 0.06 |
| Total                          | 99.05  | 99.07   | 99.58            | 99.65 | 99.75 | 99.81            | 0.32 | 100.14               | 99.86  | 99.52 | 99.81            | 0.28 |

\* All iron is calculated as Fe<sub>2</sub>O<sub>3</sub>; n = number of analyses; n.a. = not analysed; n.d. = not detected; S = standard deviation.

**Table 2.** Trace and rare earth element composition (in ppm) of representative mud masses from the Bulganak mud volcano area in comparison with Middle and Upper Maykop shales (Kerch-Taman MV province).

| Rock   | Middle | Upper   | Fresh Mud Masses |       |       |                  |      | Weathered Mud Masses |        |       |                  |      |
|--------|--------|---------|------------------|-------|-------|------------------|------|----------------------|--------|-------|------------------|------|
|        | Maykop | Maykop  |                  |       |       |                  |      |                      |        |       |                  |      |
| Sample | T-1-3  | BT-18-1 | B-3-4            | O-1-2 | 202-2 | Mean<br>(n = 10) | S    | B-3-7                | 203-1s | 203-2 | Mean<br>(n = 11) | S    |
| Li     | n.a.   | 56.6    | 103              | 65.6  | 69.0  | 82.5             | 23.4 | 82.8                 | 77.5   | 62.6  | 68.9             | 13.7 |
| Be     | n.a.   | 2.16    | 1.85             | 1.68  | 1.70  | 1.75             | 0.18 | 1.86                 | 1.91   | 1.83  | 1.84             | 0.06 |
| B      | n.a.   | 61.4    | 746              | 602   | 638   | 837              | 369  | 549                  | 993    | 598   | 810              | 278  |
| Sc     | 18.7   | 20.7    | 17.3             | 17.7  | 15.5  | 16.6             | 2.91 | 18.9                 | 17.5   | 17.7  | 18.2             | 0.68 |
| V      | 123    | 158     | 111              | 102   | 101   | 107              | 14.3 | 123                  | 125    | 115   | 116              | 10.8 |
| Cr     | 145    | 125     | 90.1             | 85.7  | 83.1  | 88.9             | 13.6 | 102                  | 104    | 94.9  | 95.2             | 10.8 |
| Mn     | 920    | 249     | 637              | 723   | 694   | 657              | 43.8 | 601                  | 621    | 758   | 665              | 70.7 |
| Co     | 19.4   | 18.2    | 20.7             | 21.5  | 19.4  | 20.7             | 2.54 | 21.9                 | 20.8   | 18.8  | 20.9             | 1.61 |
| Ni     | 76.0   | 45.9    | 49.0             | 42.6  | 43.9  | 45.7             | 5.03 | 50.6                 | 49.0   | 44.2  | 47.2             | 3.10 |
| Cu     | 41.7   | 38.1    | 24.1             | 23.8  | 22.2  | 22.9             | 2.26 | 24.6                 | 25.7   | 24.4  | 24.9             | 0.57 |
| Zn     | 87.0   | 112     | 94.8             | 134   | 114   | 116              | 22.7 | 131                  | 114    | 112   | 123              | 11.1 |
| Ga     | n.a.   | 19.4    | 14.1             | 12.9  | 12.6  | 13.5             | 1.88 | 15.5                 | 15.5   | 14.4  | 14.6             | 1.21 |
| Ge     | n.a.   | 1.30    | 1.20             | 1.13  | 0.96  | 1.03             | 0.11 | 1.04                 | 0.93   | 0.88  | 0.95             | 0.07 |
| As     | n.a.   | 27.2    | 22.3             | 22.5  | 12.7  | 20.5             | 4.84 | 13.6                 | 15.9   | 14.6  | 19.6             | 9.86 |
| Se     | n.a.   | 8.69    | 3.72             | 5.54  | 4.17  | 4.73             | 1.37 | 4.38                 | 5.43   | 5.89  | 5.00             | 0.78 |
| Rb     | 86.3   | 95.0    | 84.7             | 75.0  | 76.0  | 80.8             | 10.3 | 91.8                 | 89.4   | 83.1  | 84.9             | 7.30 |
| Sr     | 182    | 89.8    | 177              | 313   | 578   | 294              | 165  | 184                  | 150    | 163   | 152              | 30.2 |
| Y      | 21.1   | 17.2    | 11.8             | 12.6  | 12.2  | 12.5             | 0.77 | 12.1                 | 12.5   | 13.8  | 13.4             | 1.38 |
| Zr     | 150    | 92.7    | 48.0             | 65.0  | 53.6  | 56.3             | 6.20 | 51.7                 | 56.8   | 59.0  | 58.3             | 5.82 |
| Nb     | 12.3   | 9.27    | 7.36             | 7.10  | 7.30  | 7.44             | 0.34 | 7.88                 | 7.42   | 7.61  | 7.58             | 0.21 |
| Mo     | 1.00   | 0.66    | 0.75             | 1.27  | 0.83  | 1.04             | 0.45 | 0.57                 | 2.97   | 1.25  | 1.45             | 1.06 |
| Cd     | 0.12   | 0.25    | 0.21             | 0.14  | 0.18  | 0.16             | 0.04 | 0.17                 | 0.20   | 0.19  | 0.19             | 0.03 |
| Sn     | n.a.   | 2.19    | 1.88             | 1.84  | 1.80  | 1.85             | 0.20 | 1.99                 | 2.00   | 1.97  | 1.91             | 0.16 |
| Sb     | 0.73   | 2.09    | 1.50             | 1.88  | 1.35  | 1.74             | 0.29 | 2.04                 | 2.07   | 1.58  | 2.09             | 0.46 |
| Cs     | 4.00   | 6.89    | 7.92             | 5.47  | 5.27  | 6.06             | 1.26 | 7.14                 | 6.41   | 5.77  | 6.05             | 0.96 |
| Ba     | 347    | 281     | 291              | 273   | 375   | 326              | 82.5 | 258                  | 264    | 268   | 271              | 16.6 |
| Hf     | 4.00   | 5.90    | 5.04             | 11.9  | 6.53  | 6.52             | 2.68 | 5.52                 | 5.30   | 6.81  | 6.03             | 0.74 |

Table 2. Cont.

| Rock | Middle Maykop Shale | Upper Maykop Shale | Fresh Mud Masses |       |         |       |       | Weathered Mud Masses |               |      |       |        |
|------|---------------------|--------------------|------------------|-------|---------|-------|-------|----------------------|---------------|------|-------|--------|
|      |                     |                    | Sample           | T-1-3 | BT-18-1 | B-3-4 | O-1-2 | 202-2                | Mean (n = 10) | S    | B-3-7 | 203-1s |
| Ta   | 3.05                | 0.36               | 0.47             | 0.37  | 0.35    | 0.39  | 0.07  | 0.41                 | 0.38          | 0.52 | 0.41  | 0.08   |
| W    | n.a.                | 0.99               | 0.82             | 1.82  | 1.50    | 1.15  | 0.43  | 1.36                 | 0.86          | 0.87 | 0.99  | 0.25   |
| Hg   | 0.06                | 0.06               | 0.54             | 0.42  | 0.47    | 0.38  | 0.15  | 0.51                 | 0.60          | 0.48 | 0.43  | 0.21   |
| Tl   | n.a.                | 0.39               | 0.29             | 0.27  | 0.27    | 0.29  | 0.02  | 0.30                 | 0.30          | 0.30 | 0.30  | 0.01   |
| Pb   | n.a.                | 17.6               | 17.0             | 15.3  | 16.0    | 16.5  | 0.69  | 16.2                 | 16.6          | 16.5 | 16.8  | 0.85   |
| Bi   | n.a.                | 0.27               | 0.19             | 0.16  | 0.17    | 0.18  | 0.02  | 0.21                 | 0.19          | 0.18 | 0.20  | 0.02   |
| Th   | 10.0                | 10.2               | 8.20             | 10.1  | 8.22    | 8.78  | 1.06  | 9.60                 | 8.73          | 9.28 | 9.15  | 0.37   |
| U    | 1.99                | 4.77               | 3.56             | 3.81  | 3.37    | 3.49  | 0.23  | 3.88                 | 3.05          | 3.93 | 3.80  | 0.53   |
| Br   | n.a.                | 11.5               | 71.0             | 41.4  | 38.7    | 47.7  | 17.1  | 7.10                 | 67.8          | 14.9 | 25.   | 28.5   |
| La   | 32.3                | 22.7               | 20.              | 19.7  | 19.9    | 20.1  | 0.89  | 20.8                 | 20.2          | 20.7 | 20.7  | 0.36   |
| Ce   | 64.3                | 52.2               | 44.1             | 42.3  | 43.7    | 43.7  | 2.25  | 46.1                 | 43.2          | 44.2 | 44.7  | 1.30   |
| Pr   | 7.26                | 5.90               | 5.19             | 5.28  | 5.20    | 5.37  | 0.31  | 5.45                 | 5.24          | 5.51 | 5.44  | 0.14   |
| Nd   | 27.0                | 20.5               | 19.9             | 19.1  | 19.8    | 19.7  | 0.51  | 21.2                 | 18.8          | 20.9 | 20.3  | 1.09   |
| Sm   | 5.49                | 4.43               | 4.34             | 3.94  | 4.02    | 4.08  | 0.13  | 4.39                 | 4.27          | 3.94 | 4.20  | 0.19   |
| Eu   | 1.14                | 1.02               | 0.93             | 0.75  | 0.87    | 0.88  | 0.07  | 0.88                 | 0.96          | 0.95 | 0.93  | 0.04   |
| Gd   | 4.55                | 3.42               | 3.42             | 3.39  | 3.46    | 3.48  | 0.15  | 3.58                 | 3.34          | 3.53 | 3.53  | 0.15   |
| Tb   | 0.68                | 0.56               | 0.47             | 0.46  | 0.49    | 0.48  | 0.03  | 0.51                 | 0.47          | 0.49 | 0.50  | 0.02   |
| Dy   | 4.07                | 3.04               | 2.77             | 2.49  | 2.52    | 2.63  | 0.12  | 2.80                 | 2.84          | 2.82 | 2.84  | 0.06   |
| Ho   | 0.83                | 0.56               | 0.51             | 0.47  | 0.46    | 0.49  | 0.03  | 0.46                 | 0.43          | 0.50 | 0.48  | 0.05   |
| Er   | 2.28                | 1.54               | 1.15             | 1.28  | 1.15    | 1.34  | 0.25  | 1.28                 | 1.29          | 1.43 | 1.37  | 0.10   |
| Tm   | 0.34                | 0.25               | 0.20             | 0.16  | 0.17    | 0.19  | 0.02  | 0.17                 | 0.18          | 0.19 | 0.19  | 0.02   |
| Yb   | 2.30                | 1.47               | 1.04             | 0.94  | 1.13    | 1.12  | 0.16  | 0.99                 | 1.13          | 1.26 | 1.21  | 0.19   |
| Lu   | 0.35                | 0.25               | 0.18             | 0.13  | 0.19    | 0.19  | 0.04  | 0.16                 | 0.14          | 0.19 | 0.16  | 0.02   |

n = number of analyses; n.a. = not analyzed; n.d. = not detected; S = standard deviation. Concentration (in ppm): 0.002 < Te ≤ 0.12, Au < 0.001, Ag < 1.

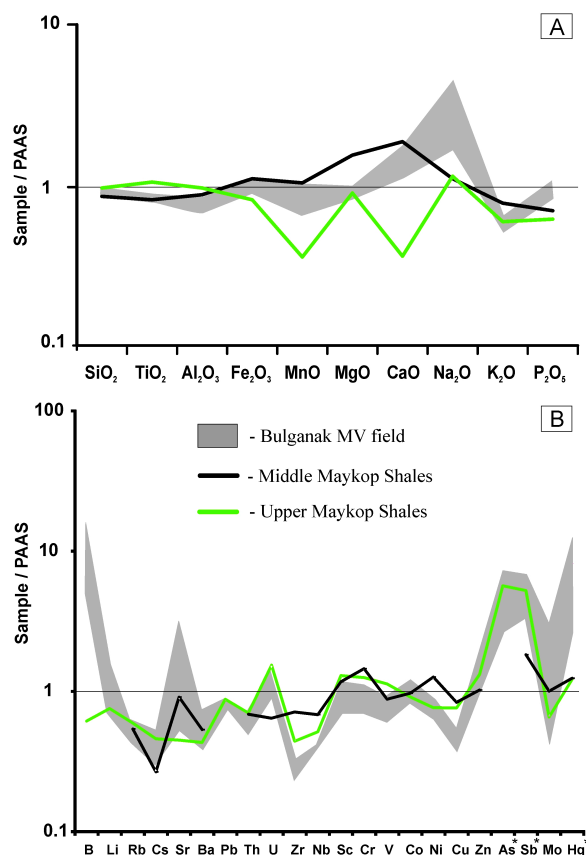


Figure 4. PAAS-normalised [75] major (A) and trace (B) element patterns of mud masses (Bulganak MV field) and Maykop parent rocks (Tables 1 and 2). \* Upper crust-normalised [76] data.

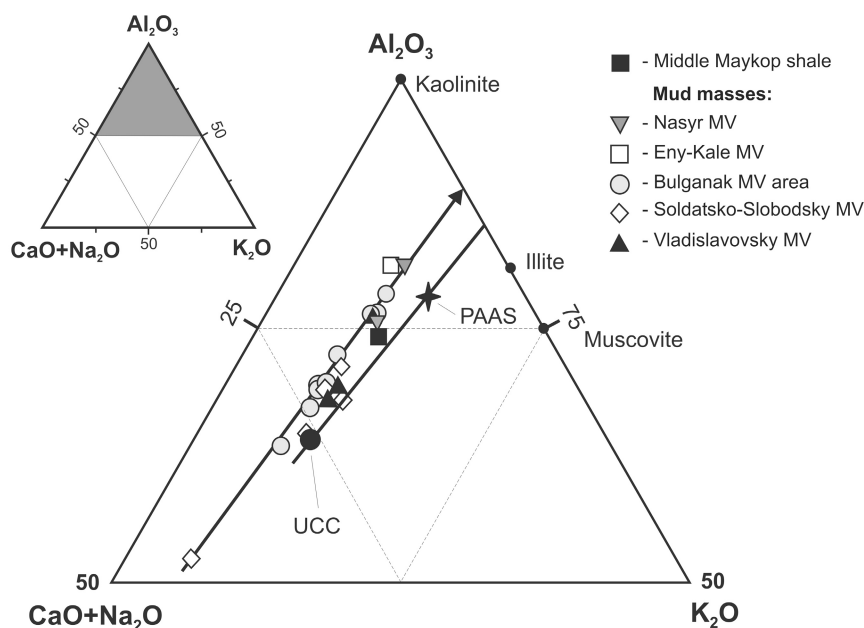


Figure 5. Chemical weathering ternary after [75].

#### 4.2. Bulk-Rock Mineralogy

The bulk MMs extruded by the Bulganak MVs consist of ~29–35 wt % quartz, ~7–11 wt % high-silica plagioclase, and 2–5 wt % potassium feldspar (sand fraction); 18–40 wt % illite and mix illite-smectite (totally); ~12–17 wt % kaolinite, ~2–4 wt % chlorite, 1–4 wt % Fe-rich carbonate, and ~1 wt % calcite. The principal minerals of the clay fraction (<2  $\mu\text{m}$ ) isolated from MMs include illite (61–73 wt %) and kaolinite (13–29 wt %) with minor amounts (<3–7 wt %) of disordered illite-smectite phases with ~30% of smectite layers. Disordered illite-smectite is more abundant (12–20 wt %) in clay fractions from other mud volcanoes in the Kerch Peninsula. Quite large (hundreds of microns) flake fragments of slightly weathered chlorite and muscovite occur in the coarse fraction but are undetectable in the diffraction patterns of the clay fraction, and rather belong to clastics transported from the provenance areas.

The Middle Maykop Shale samples from the Azov coastal outcrop share general similarity with Bulganak MMs in bulk mineralogy, but their clay fraction stores lower amounts of both illite (54–64 wt %) and kaolinite (5–11 wt %) and higher amounts of disordered illite-smectite (11–15 wt %). They also may contain up to 2 wt % pyrite and/or 4 wt % biogenic calcite and aragonite; <1 wt % Fe-rich carbonate restricted to a few layers; and sporadic glauconite pellets. The exposed sediments are cut by numerous veins of gypsum or jarosite and store partially oxidised opaque minerals. As a consequence, the heavy fraction contains abundant Fe-(oxy)hydroxides.

The mineralogy of heavy clastic fractions from the MMs and Middle Maykop shales of the area is generally uniform, with a predominant assemblage of ultrastable minerals which are most resistant to weathering, dissolution and transport. The HM assemblages of all studied samples mainly contain fine-grained well-rounded, fragments of rutile, ilmenite, kyanite, sillimanite, garnets and some andalusite. Well-rounded grains of zircon, titanite, magnetite, tourmaline, monazite, apatite and Cr-spinel are sporadic. Subangular epidote grains predominate among non-resistant HM, while amphiboles and pyroxenes are angular and few. The Bulganak mud contains lower percentages of non-resistant HM than the Middle Maykop shales. All sediments also bear clots of Fe-(oxy)hydroxides composed of amorphous matter and goethite. Fe-(oxy)hydroxides may also occur as films over fine-grained quartz-Fe-carbonate ( $\pm$ pyrite) aggregates. The ratio of  $\text{FeS}_2/\text{Fe-(oxy)hydroxides}$  in the heavy fraction from the Middle Maykop shale reduces to 1:2, mainly because of supergene oxidation and hydration of sulphides, which impedes reliable identification of authigenic mineralization.

Authigenic mineral assemblages are diverse, but all MM samples we studied contain predominant Fe(Mn)-rich carbonates, abundant pyrite and authigenic quartz, as well as some marcasite, glauconite, and barite found as separate crystals and complex intergrowths (Table 3, Figures 6–9). Pyrite is the most abundant authigenic mineral in the Middle Maykop shale, marcasite crystals are also common, whereas Fe-bearing calcite and oligonite do not exceed 10% of sulphides. The MM aggregates of Fe and Mn-rich mix carbonates, as well as pyrite, commonly contain minor clayey matter; rarely siderite is found grown together with glauconite pellets (Figure 9g,h). Compositionally similar carbonates (siderite, ankerite, oligonite) are frequently intergrown, while aggregation of different carbonate species is rare (Figure 6). Fine-crystalline siderite often coexists with Fe-(oxy)hydroxides and more rarely with framboidal pyrite (Figure 9f), while only fine pyrite particles are present on the faces of larger rhombohedral crystals. Some Fe-carbonates coexist with gypsum (Figure 9e,f), Fe-(oxy)hydroxides, and with fine clots of authigenic apatite. The aggregates of authigenic carbonates and pyrite contain silica, either as clots, a sort of cement or, rarely, as euhedral fine crystals (Figures 6b and 9i). The XRD analysis failed to identify polymorphic SiO<sub>2</sub> modifications other than quartz.

Barite forms stellar and fibrous aggregates, or rarely intergrowths or irregular grains coexisting with pyrite and occasionally with sphalerite. The mineral fills cracks in large pyrite crystals, as well as the space between pyrite framboids. Barite rarely contains up to 2.18 wt % SrO. Celestine (with 6.30–7.45 wt % BaO) is rare and mostly occurs in rims around barite (Figure 9a–c). Gypsum is very rare, found as aggregates of anhedral grains (<2 μm in size) that coat fine intergrowths of authigenic silica, siderite, and pyrite (Figure 9d–f).

**Table 3.** Authigenic minerals identified in the heavy fraction of the mud masses from Bulganak MV area (optical microscopy, SEM, XRD and EMPA).

| Phase   | Mud Volcano Hill |          |            |
|---|------------------|----------|------------|
|   | Tischenko        | Andrusov | Trubetskoy |
| <i>Carbonates</i>   |                  |          |            |
| Siderite ((Fe,Mg)CO <sub>3</sub> )  | ◆                | ◆        | ◆          |
| Ankerite (Ca(Fe <sup>2+</sup> ,Mg)(CO <sub>3</sub> ) <sub>2</sub> )   | ▲                | ▲        | ▲          |
| Dolomite (CaMg(CO <sub>3</sub> ) <sub>2</sub> )   | ●                | ●        | ●          |
| Calcite (CaCO <sub>3</sub> )  |                  |          | ●          |
| Oligonite (Fe,Mn,Mg,Ca)CO <sub>3</sub>  | ●                |          |            |
| Kutnohorite (Ca(Mn,Mg,Fe <sup>2+</sup> )(CO <sub>3</sub> ) <sub>2</sub> )   | ●                |          |            |
| Mn-calcite ((Ca,Mn)CO <sub>3</sub> )  |                  |          | ●          |
| Ca-rhodochrosite ((Mn,Ca)CO <sub>3</sub> )  |                  | ●        |            |
| <i>Sulphides</i>  |                  |          |            |
| Pyrite (FeS <sub>2</sub> )  | ◆                | ◆        | ◆          |
| Marcasite (FeS <sub>2</sub> )   | ●                | ●        | ▲          |
| Cinnabar (HgS)  |                  | ●        |            |
| Sphalerite (ZnS)  |                  | ▲        |            |
| Cu <sub>5</sub> FeS <sub>6</sub>  | ●                |          |            |
| Chalcopyrite (CuFeS <sub>2</sub> )  | ●                |          |            |
| Akantite α-Ag <sub>2</sub> S  |                  | ●        |            |
| Pb-S-bearing phase  | ●                |          |            |
| <i>Native elements and alloys</i>   |                  |          |            |
| Copper (Cu <sup>0</sup> )   | ●                |          |            |
| Gold (Au <sup>0</sup> )   | ●                |          |            |
| Gold-Silver alloy (Au <sub>x</sub> Ag <sub>1-x</sub> )  | ●                |          |            |
| <i>Sulphates</i>  |                  |          |            |
| Barite (BaSO <sub>4</sub> )   | ●                | ●        | ●          |
| Celestine (SrSO <sub>4</sub> )  |                  |          | ●          |
| Gypsum (CaSO <sub>4</sub> ·2H <sub>2</sub> O)   | ●                | ●        |            |
| <i>Oxydes/(oxy)hydroxides</i>   |                  |          |            |
| Fe(Mn)-(oxy)hydroxides  | ▲                | ▲        | ▲          |
| Quartz (SiO <sub>2</sub> )  | ▲                | ▲        | ▲          |
| <i>Silicates</i>  |                  |          |            |
| Glauconite<br>(K,Na)(Fe <sup>3+</sup> ,Fe <sup>2+</sup> ,Al,Mg) <sub>2</sub> (Si,Al) <sub>4</sub> O <sub>10</sub> (OH) <sub>2</sub> | ●                | ●        | ●          |

◆ = abundant phase (>10 vol %), ▲ = rare phase (1–10 vol %), ● = accessory phase (<1 vol %), not filled cell = absent.

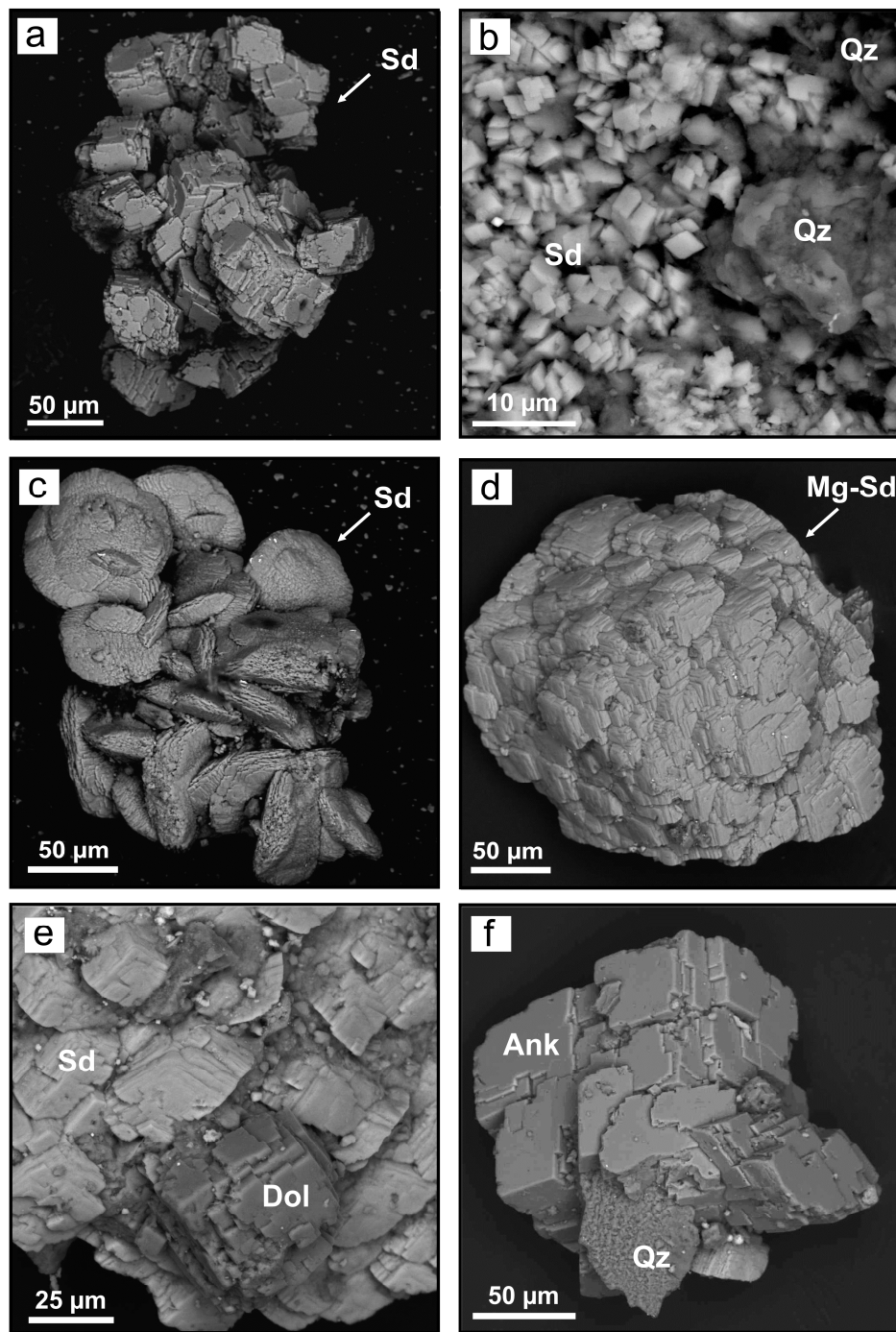


**Figure 6.** Morphology of authigenic carbonates from mud masses (Bulganak area). (a) Large rhombohedral crystals of siderite with rough faces and distinct growth steps; (b) Intergrowth of fine-grained siderite and quartz. Siderite forms tiny rhombohedral crystals with flat faces and well-defined edges and corners. Quartz exists as clots with uneven surface or as cement filling voids between siderite grains; (c) Foliated rhombohedrons of siderite; (d) Large rhombohedral crystal of Mg-siderite with intricately sculptured faces laminae and smoothed edges and corners; (e) Intergrowth of rhombohedral siderite and dolomite; crystals have rough faces with distinct growth steps; (f) Rhombohedral ankerite crystal with rough growth steps. Ankerite forms intergrowth with quartz. Back-scattered electron (BSE) images. Ank = ankerite; Dol = dolomite; Mg-Sd = magnesian siderite; Sd = siderite; Qz = quartz. (a,b) = Tischenko Hill; (c-f) = Trubetskoy Hill.

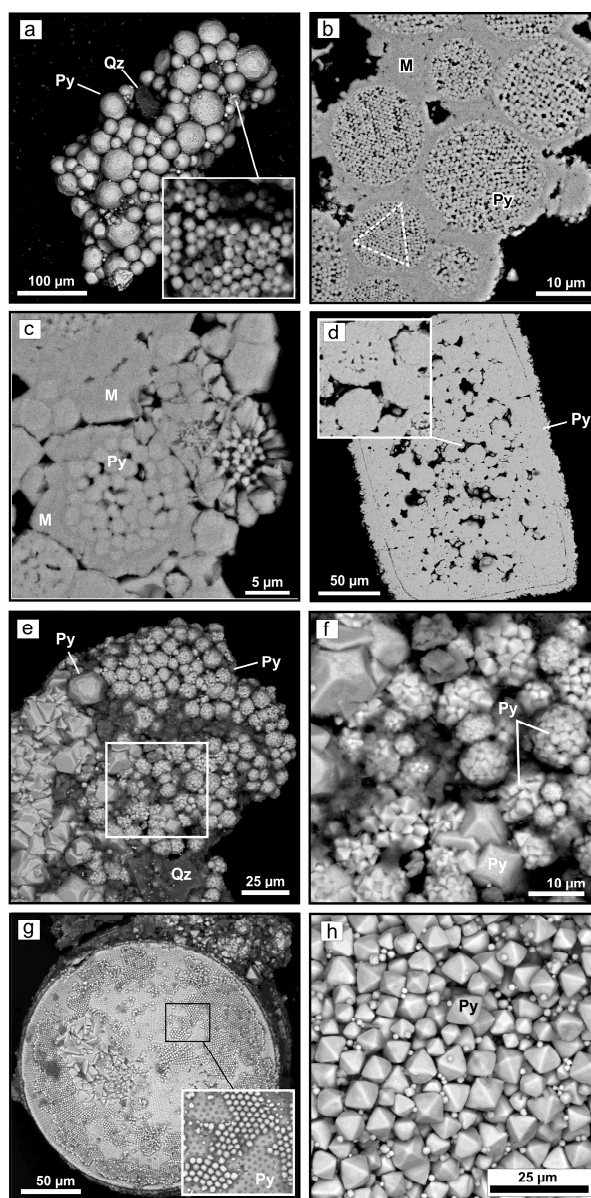


**Figure 7.** Morphology of primary and recrystallised pyrite framboids from mud masses (Bulganak area). (a) Botryoidal aggregate of primary spherical framboids and partly recrystallised framboids that acquire cubo-octahedral habits. Most framboids are ordered (sometimes with shared microcryst orientation) and filled. Crystallites comprising framboids are mostly cubo-octahedral (b) Botryoidal aggregate of primary spherical framboids buried in matrix. Most framboids are ordered and filled. One framboid has trigonal symmetry. Framboid crystallites are octahedral and cubo-octahedral; (c) Sunflower structures with framboidal core rimmed by radiating outer crystals (on the right) and partly recrystallised framboids buried in matrix; (d) Recrystallised framboids composing a pseudomorph after a fossil remnant. Framboids that preserve discrete crystallites separated by holes in the core and rimmed by massive aggregates of agglomerated crystallites correspond to early recrystallisation. Completely filled spherules correspond to a more progressive stage of recrystallisation; (e,f) Intergrowth of primary spherical framboids (on the right) and cubo-octahedral pyrite crystals formed during recrystallisation of framboids (on the left). Framboids consist of octahedral and cubo-octahedral crystallites (f); (g,h) Aggregate of octahedral and cubo-octahedral crystals that formed during final stage of framboids recrystallisation. Crystals compose a pseudomorph after a fossil remnant and are buried in the matrix (g). BSE images. M = matrix; Py = pyrite; Qz = quartz. (a,c,d) = Tischenko Hill; (b,g) = Andrusov Hill; (e,f,h) = Trubetskoy Hill.

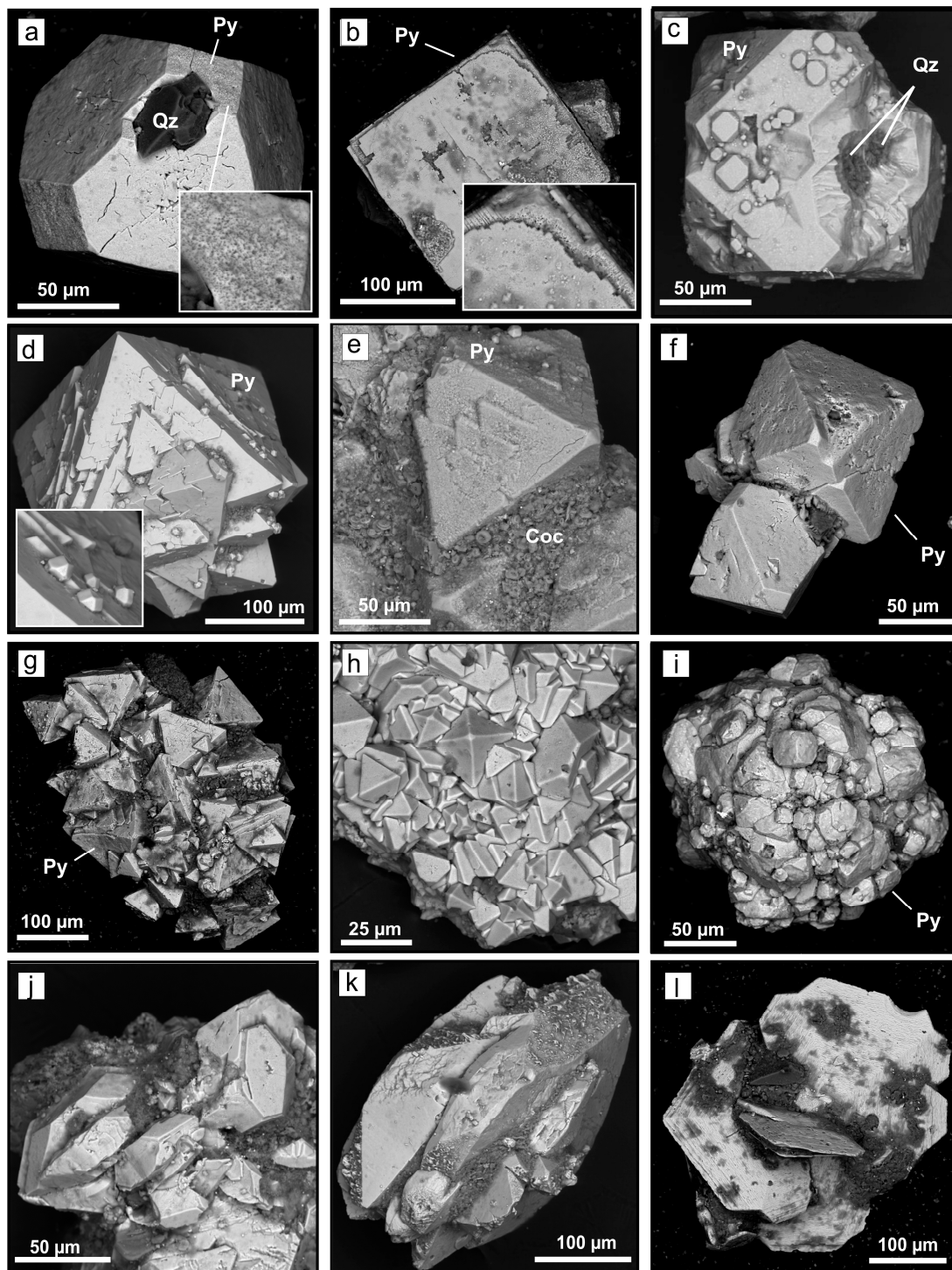


**Figure 8.** Morphology of large pyrite (a–i) and marcasite (j–l) crystals from mud masses (Bulganak area). (a) Cubo-octahedral pyrite crystal. Some faces are heavily etched; (b,c) Cubic ( $\{100\}$ ) crystals. Crystal faces are heavily etched (b), have stepped growth layers (c) and are dusted with microcrystals of later generations (b,c). Some crystals show  $\{111\}$  faces (c); (d–h) Octahedral ( $\{111\}$ ) crystals and their aggregates. Some crystal faces are heavily etched (e–g), have screw dislocations (d,g) and are dusted with microcrystals of later generations (d). Pyrite coexists with coccoliths (e), clay and quartz (f,g); (i) Rounded aggregate of cubo-octahedral crystals ( $\{100\}$  faces are dominated). Some octahedral faces are heavily etched; (j,k) Tabular (flattened on  $(010)$ ) and prismatic crystals of marcasite coexisting with clay and quartz; (l) Twins of marcasite coexisting with clay and quartz. BSE images. Coc = coccoliths; Py = pyrite; Qz = quartz. (a,b,i,l) = Tischenko Hill; (c–e,h,j,k) = Trubetskoy Hill; (f,g) = Andrusov Hill.

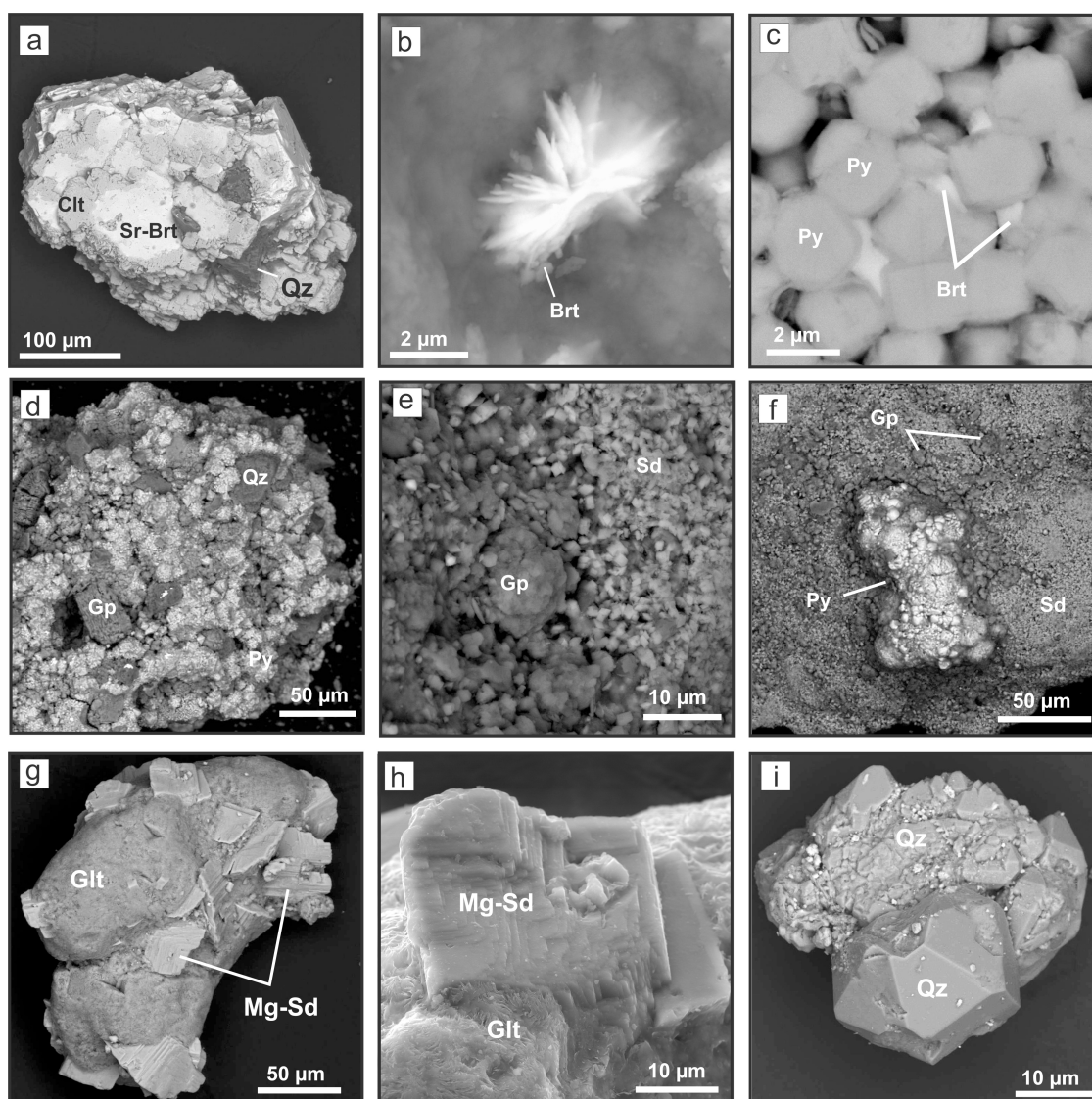


**Figure 9.** Morphology of sulphates, glauconite and quartz from mud masses (Bulganak area). (a) Intergrowth of Sr-barite, celestine and quartz. Celestine forms rims around earlier Sr-barite; (b) Star-like aggregate of barite; (c) Barite filling space between pyrite crystallites; (d) Prismatic gypsum crystals coexisting with recrystallised pyrite framboids and quartz; (e,f) Granular aggregates of unfaceted gypsum grains covering intergrowths of fine-grained siderite and recrystallised pyrite; (g,h) Intergrowth of rhombohedral Mg-siderite and glauconite pellets. Mg-siderite crystals have rough faces. Glauconite pellets are composed of aggregate of overlapping micaceous flakes with no preferred orientation; (i) Quartz euhedral crystals. BSE images. Brt = barite; Sr-Brt = Sr-barite; Clt = celestine; Glt = glauconite; Gp = gypsum; Py = pyrite; Qz = quartz; Sd = siderite. (a,b) = Trubetskoy Hill; (c,g,h,i) = Andrusov Hill; (d–f) = Tischenko Hill.

### 4.3. Authigenic Mineralogy and Mineral Chemistry

#### 4.3.1. Carbonates: Morphology, Chemistry, and Isotopes

$\text{FeCO}_3$ -rich solid solutions and ankerite are the principal authigenic phases in the heavy fraction of the Bulganak MMs. Mn-rich carbonates are of limited occurrence and dolomite is very rare (Tables 3 and 4, Figure 10). Most calcite resides in foraminiferal tests.

Table 4. Representative EMPA analyses of authigenic carbonates from mud masses.

| Mineral              | CaO   | FeO   | MgO   | MnO   | Na <sub>2</sub> O | SrO  | ZnO  | Total | FeCO <sub>3</sub> | MgCO <sub>3</sub> | CaCO <sub>3</sub> | MnCO <sub>3</sub> |
|----------------------|-------|-------|-------|-------|-------------------|------|------|-------|-------------------|-------------------|-------------------|-------------------|
|                      |       |       |       |       |                   |      |      |       |                   |                   |                   |                   |
| LLD                  | 0.01  | 0.01  | 0.03  | 0.01  | 0.02              | 0.02 | 0.02 |       |                   |                   |                   |                   |
| Tischenko hill       |       |       |       |       |                   |      |      |       |                   |                   |                   |                   |
| Sd *                 | 4.43  | 49.85 | 3.13  | 0.33  | 0.18              | bdl  | bdl  | 57.95 | 81                | 9                 | 9                 | 1                 |
| Sd                   | 5.23  | 44.90 | 7.50  | 0.07  | 0.06              | 0.06 | bdl  | 57.82 | 70                | 20                | 10                | 0                 |
| Sd                   | 5.97  | 49.16 | 2.97  | 0.43  | 0.14              | 0.06 | 0.12 | 58.85 | 79                | 8                 | 12                | 1                 |
| Sd                   | 7.31  | 46.99 | 2.40  | 0.82  | 0.08              | 0.09 | 0.12 | 57.81 | 77                | 7                 | 15                | 1                 |
| Sd                   | 5.19  | 39.65 | 10.47 | 1.50  | 0.15              | 0.06 | bdl  | 57.04 | 60                | 28                | 10                | 2                 |
| Sd                   | 1.19  | 40.03 | 11.07 | 6.51  | 0.13              | bdl  | 0.05 | 58.98 | 59                | 29                | 2                 | 10                |
| Olig *               | 4.41  | 29.02 | 8.75  | 14.42 | 0.11              | 0.05 | 0.19 | 56.96 | 44                | 25                | 9                 | 22                |
| Olig *               | 5.80  | 24.29 | 6.77  | 21.28 | 0.18              | bdl  | 0.15 | 58.54 | 37                | 19                | 11                | 33                |
| Olig *               | 5.15  | 25.16 | 7.86  | 20.70 | 0.10              | 0.07 | 0.14 | 59.18 | 38                | 21                | 10                | 31                |
| Kut                  | 22.86 | 1.96  | 6.84  | 25.71 | 0.22              | 0.06 | bdl  | 57.70 | 3                 | 18                | 42                | 37                |
| Dol                  | 29.47 | 5.62  | 17.28 | bdl   | bdl               | bdl  | bdl  | 52.37 | 8                 | 42                | 50                | 0                 |
| Andrusov hill        |       |       |       |       |                   |      |      |       |                   |                   |                   |                   |
| Sd *                 | 4.61  | 49.48 | 1.95  | 0.39  | 0.23              | bdl  | 0.10 | 56.80 | 83                | 6                 | 10                | 1                 |
| Sd                   | 6.38  | 50.15 | 0.55  | 0.83  | 0.23              | bdl  | bdl  | 58.17 | 84                | 2                 | 13                | 1                 |
| Sd                   | 4.26  | 47.89 | 4.66  | 0.93  | 0.18              | 0.09 | bdl  | 58.04 | 77                | 13                | 9                 | 1                 |
| Sd <sup>1</sup>      | 5.07  | 45.43 | 7.40  | 0.38  | bdl               | 0.08 | 0.08 | 58.52 | 69                | 20                | 10                | 1                 |
| Sd                   | 4.89  | 45.63 | 7.80  | 0.39  | 0.06              | bdl  | 0.12 | 58.91 | 69                | 21                | 9                 | 1                 |
| Ank                  | 33.04 | 13.33 | 11.33 | 0.24  | bdl               | bdl  | bdl  | 57.99 | 18                | 26                | 55                | 1                 |
| Ank                  | 31.72 | 11.22 | 13.35 | 0.15  | bdl               | 0.09 | bdl  | 56.56 | 15                | 32                | 53                | 0                 |
| Ank                  | 31.59 | 11.91 | 13.21 | 0.19  | bdl               | 0.25 | bdl  | 57.21 | 16                | 30                | 54                | 0                 |
| Ca-Rhod <sup>2</sup> | 15.10 | 1.27  | 0.75  | 40.47 | 0.12              | bdl  | bdl  | 57.88 | 2                 | 2                 | 30                | 66                |
| Trubetskoy hill      |       |       |       |       |                   |      |      |       |                   |                   |                   |                   |
| Sd *                 | 5.16  | 48.44 | 4.35  | 0.48  | 0.17              | bdl  | 0.07 | 58.67 | 76                | 12                | 10                | 1                 |
| Sd                   | 9.75  | 41.93 | 2.17  | 4.37  | 0.20              | bdl  | 0.06 | 58.53 | 66                | 6                 | 20                | 7                 |
| Sd                   | 1.58  | 46.23 | 10.65 | 0.25  | bdl               | bdl  | bdl  | 58.74 | 68                | 28                | 3                 | 0                 |
| Ank                  | 31.57 | 9.47  | 15.54 | 0.20  | bdl               | 0.17 | bdl  | 56.97 | 12                | 35                | 52                | 1                 |
| Ank                  | 31.53 | 12.70 | 12.27 | 0.26  | 0.05              | 0.41 | bdl  | 57.22 | 17                | 29                | 53                | 1                 |
| Ank                  | 31.66 | 13.81 | 11.21 | 0.17  | bdl               | 0.10 | bdl  | 57.00 | 19                | 26                | 55                | 0                 |
| Mn-Cal               | 31.64 | 0.33  | 0.15  | 26.04 | 0.08              | 0.05 | bdl  | 58.31 | 1                 | 1                 | 59                | 39                |
| Cal <sup>3</sup>     | 52.29 | 1.95  | 0.40  | 0.19  | bdl               | 0.08 | bdl  | 54.98 | 3                 | 1                 | 96                | 0                 |
| Dol                  | 28.85 | 5.84  | 17.83 | 1.10  | bdl               | bdl  | bdl  | 53.62 | 8                 | 42                | 48                | 2                 |

LLD = lower limit of detection; bdl = below detection limit. Concentrations of BaO: <sup>1</sup>—0.08 wt %; <sup>2</sup>—0.12 wt %; <sup>3</sup>—0.07 wt %; other samples < 0.03 wt % (LLD). \* grain size < 5 µm; other grains are 10–300 µm. Ank = ankerite, Cal = calcite, Ca-Rhod = Ca-rhodochrosite, Dol = dolomite, Kut = kutnohorite, Mn-Cal = Mn-calcite, Olig = oligonite, Sd = siderite.

Siderite predominantly occurs as intergrowths of tiny rhombohedral crystals ( $\leq 5$  µm) or less often as separate and aggregated large rhombohedra (up to 300 µm) (Figure 6). The tiny rhombohedra have flat faces and well-defined edges and corners (Figure 6a), while the larger crystals are commonly obtuse rhombohedra (Figure 6a,c–e) with intricately sculptured faces (tile-like) and often rounded edges and corners; some siderite crystals are hollow case-like or massive. The morphologically similar siderite crystals in different samples show no systematic compositional difference. The tiny crystals commonly contain 75–83 mol % FeCO<sub>3</sub> and  $\leq 1$  mol % MnCO<sub>3</sub>; with both CaCO<sub>3</sub> and MgCO<sub>3</sub> contents of about 10 mol % (Table 4). Larger rhombohedra are richer in MgCO<sub>3</sub> (up to 20–29 mol %); CaCO<sub>3</sub> (20 mol %), and MnCO<sub>3</sub> (7–10 mol %). All siderites contain impurities: up to 0.35 wt % Na<sub>2</sub>O, 0.12 wt % ZnO, and 0.13 wt % SrO.

Ankerite (52–55 mol % CaCO<sub>3</sub>, 26–35 mol % MgCO<sub>3</sub>, 12–19 mol % FeCO<sub>3</sub>, and  $\leq 1$  mol % MnCO<sub>3</sub>) (Table 4) occurs as aggregates of fine grains or larger rhombohedral crystals with complex rough face surfaces, blunt edges and corners (Figure 6f).

Mn carbonates are coarse crystals of kutnohorite, Mn-calcite and Ca-rhodochrosite and fine-grained clots of mix carbonates (oligonite), with high contents of FeCO<sub>3</sub> (37–44 mol %), MnCO<sub>3</sub> (22–33 mol %), MgCO<sub>3</sub> (19–25 mol %) and low CaCO<sub>3</sub> (9–12 mol %) (Table 4).

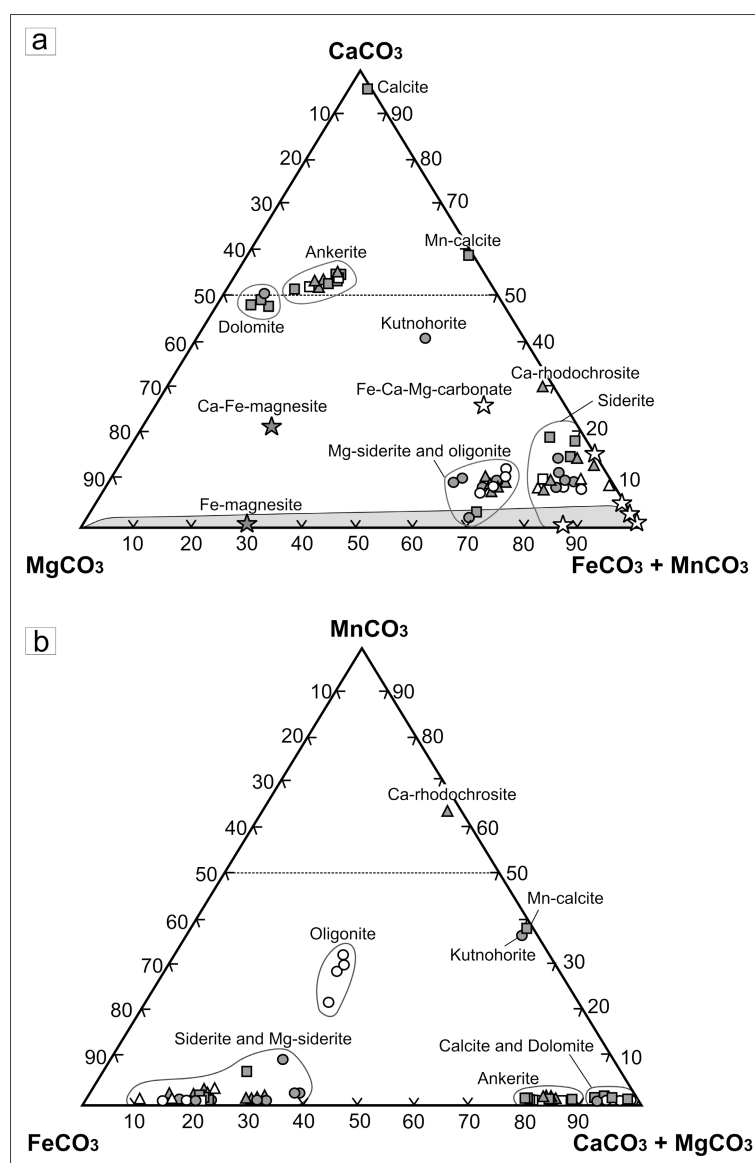


**Figure 10.** Triangular diagrams: (a) CaCO<sub>3</sub>-MgCO<sub>3</sub>-(FeCO<sub>3</sub> + MnCO<sub>3</sub>) and (b) FeCO<sub>3</sub> -MnCO<sub>3</sub>-(CaCO<sub>3</sub> + MgCO<sub>3</sub>) showing the composition of authigenic carbonates from mud masses (Bulganak area). Triangles—Andrusov Hill, squares—Trubetsky Hill, circles—Tischenko Hill; open symbols—fine-grained carbonates ( $\leq 5 \mu\text{m}$ ), filled symbols—large carbonate crystals ( $>10 \mu\text{m}$ ). Asterisks are compositions of carbonates synthesized at 25 °C (open symbols) and 70 °C (filled symbols) [77]. Shaded field corresponds to siderite-magnesite solid solutions synthesized at 250 °C [78].

Dolomite (CaMg(CO<sub>3</sub>)<sub>2</sub>) forms sporadic quite coarse rhombohedra (with 42–45 mol % MgCO<sub>3</sub>, 5–8 mol % FeCO<sub>3</sub>, and <2 mol % MnCO<sub>3</sub>) (Figure 6e). Few calcite rhombohedra (with <3 mol % FeCO<sub>3</sub>, MgCO<sub>3</sub>, and MnCO<sub>3</sub>) were found in MMs from Trubetsky Hill only.

The bulk fractions of Fe(Mn)-rich carbonates host Mn (1.53–1.73 wt %), Zn (237–439 ppm), Sr (217–278 ppm) and Ba (260–327 ppm). Their PAAS-normalised REE patterns show LREE (La, Ce, Pr, Nd) depletion relative to HREE (Er, Tm, Yb, Lu) ((LREE/HREE)<sub>SN</sub> = 0.30–0.49) (Figure 11). This is the only seawater-like signature of REE distribution typical of authigenic Fe(Mn)-rich carbonates, which lack other features, such as negative Ce or positive Y/Ho anomalies, and thus can be inferred to have formed in an oxygen-deficient environment [79,80].

The  $\delta^{13}\text{C}$  and  $\delta^{18}\text{O}$  values were measured in hand-picked siderite and ankerite fractions from Andrusov and Trubetskoy Hills, and in siderite and oligonite fractions from Tischenko Hill. Siderites are markedly enriched in  $^{18}\text{O}$ , with  $\delta^{18}\text{O}$  from +5.2‰ VPDB (36.2‰ VSMOW) to +5.9‰ VPDB (36.9‰ VSMOW), but ankerite and oligonite have lower  $\delta^{18}\text{O}$  values (+1.0‰ to +1.8‰ VPDB). The  $\delta^{13}\text{C}$  values in all studied carbonates vary between +2.1‰ and +3.7‰ VPDB. Siderite from Trubetskoy Hill has the heaviest C isotope composition (+3.5 to +3.7‰ VPDB). All authigenic carbonates are drastically different from the isotopically heavy travertines of the Big Tarkhan springs ( $\delta^{13}\text{C}_{\text{av}} = +11.8$  to +12.5‰ VPDB;  $\delta^{18}\text{O}_{\text{av}} = +10.5$  to +12.0‰ VPDB) (Table 5).

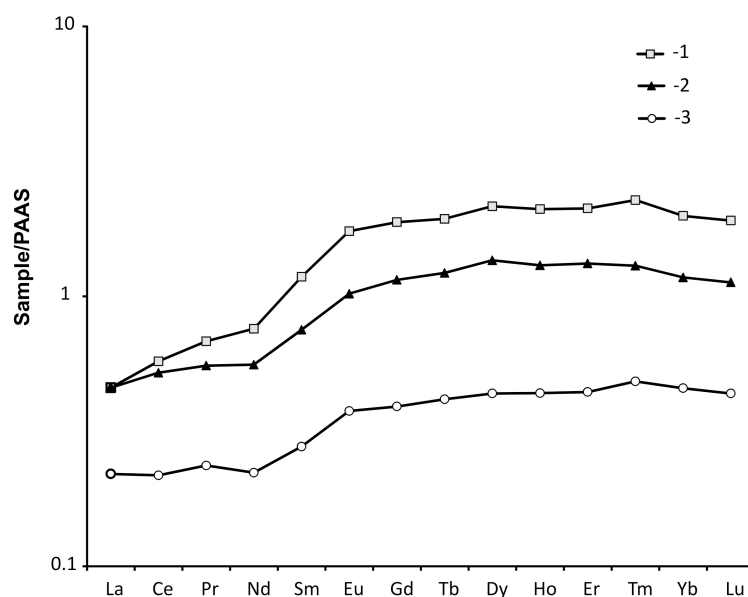


**Figure 11.** PAAS-normalised [75] REE patterns of fine-crystalline siderite (1), crystalline siderite (2), and ankerite (3) fractions from mud masses (Bulganak area).

**Table 5.** Isotope composition of authigenic carbonates and pyrite from mud masses (Bulganak MV areas) in comparison with Big Tarkhan travertine.

| Location           | Mineral             | $\delta^{13}\text{C}$<br>(VPDB), ‰ | $\delta^{18}\text{O}$<br>(VPDB), ‰ | $\delta^{18}\text{O}$<br>(VSMOW), ‰ | $\delta^{34}\text{S}$<br>(CDT), ‰ |
|--------------------|---------------------|------------------------------------|------------------------------------|-------------------------------------|-----------------------------------|
| Andrusov hill      | Ankerite            | +2.1 ± 0.1                         | +1.9 ± 0.2                         | +32.8 ± 0.2                         |                                   |
| Andrusov hill      | Ankerite            | +2.2 ± 0.1                         | +1.8 ± 0.2                         | +32.7 ± 0.2                         |                                   |
| Trubetskoy hill    | Ankerite            | +2.2 ± 0.1                         | +1.0 ± 0.2                         | +31.9 ± 0.2                         |                                   |
| Trubetskoy hill    | Ankerite            | +2.0 ± 0.1                         | +1.2 ± 0.2                         | +32.1 ± 0.2                         |                                   |
| Tischenko hill     | Oligonite           | +2.8 ± 0.1                         | +1.3 ± 0.2                         | +32.2 ± 0.2                         |                                   |
| Andrusov hill      | Siderite            | +3.3 ± 0.1                         | +5.9 ± 0.2                         | +36.9 ± 0.2                         |                                   |
| Trubetskoy hill    | Siderite            | +3.5 ± 0.1                         | +5.2 ± 0.2                         | +36.2 ± 0.2                         |                                   |
| Trubetskoy hill    | Siderite            | +3.7 ± 0.1                         | +5.5 ± 0.2                         | +36.5 ± 0.2                         |                                   |
| Tischenko hill     | Siderite            | +3.7 ± 0.1                         | +5.4 ± 0.2                         | +36.4 ± 0.2                         |                                   |
| Big Tarkhan spring | Calcite *           | +8.1 ± 0.1                         | +11.0 ± 0.2                        | +42.3 ± 0.2                         |                                   |
| Big Tarkhan spring | Calcite *           | +10.7 ± 0.1                        | +12.7 ± 0.2                        | +44.0 ± 0.2                         |                                   |
| Big Tarkhan spring | Calcite *           | +11.6 ± 0.1                        | +12.8 ± 0.2                        | +44.1 ± 0.2                         |                                   |
| Big Tarkhan spring | Calcite *           | +12.1 ± 0.1                        | +12.9 ± 0.2                        | +44.2 ± 0.2                         |                                   |
| Andrusov hill      | Pyrite framboids    |                                    |                                    |                                     | +8.94 ± 0.15                      |
| Andrusov hill      | Pyrite crystals     |                                    |                                    |                                     | +8.23 ± 0.15                      |
| Andrusov hill      | Pyrite crystals     |                                    |                                    |                                     | +6.23 ± 0.15                      |
| Trubetskoy hill    | Pyrite framboids ** |                                    |                                    |                                     | +7.40 ± 0.15                      |
| Trubetskoy hill    | Pyrite framboids ** |                                    |                                    |                                     | +5.65 ± 0.15                      |
| Trubetskoy hill    | Pyrite crystals     |                                    |                                    |                                     | +4.02 ± 0.15                      |
| Trubetskoy hill    | Pyrite crystals     |                                    |                                    |                                     | +4.18 ± 0.15                      |
| Tischenko hill     | Pyrite framboids ** |                                    |                                    |                                     | +0.38 ± 0.15                      |
| Tischenko hill     | Pyrite crystals     |                                    |                                    |                                     | +0.36 ± 0.15                      |
| Tischenko hill     | Pyrite framboids    |                                    |                                    |                                     | −1.53 ± 0.15                      |

\* After [59]; \*\* pseudomorphs after fossil organic remnant.

### 4.3.2. FeS<sub>2</sub>: Morphology

Marcasite occurs as intergrowths of tabular (flattened on (010)) and prismatic crystals or twins 25–200 μm in size (Figure 8i,j).

Pyrite has several common modes of occurrence in MMs: (1) botryoidal aggregates of framboids, sometimes partly recrystallised; (2) pseudomorphs after fossil organic remnants composed of framboids; (3) coarse (up to 200 μm) euhedral crystals and their intergrowths (Figures 7 and 8). Pyrite is often intergrown with Fe-rich authigenic carbonates and quartz (both sandy and authigenic), less often with Fe-(oxy)hydroxides, and very rarely with gypsum (Figures 8e and 9d,f), metallic copper and akantite (Figure 12e,i). The space between crystals and framboids is often filled with clayey matter, or occasionally with some fine authigenic apatite, barite, and very rare coccolith (Figure 9c).

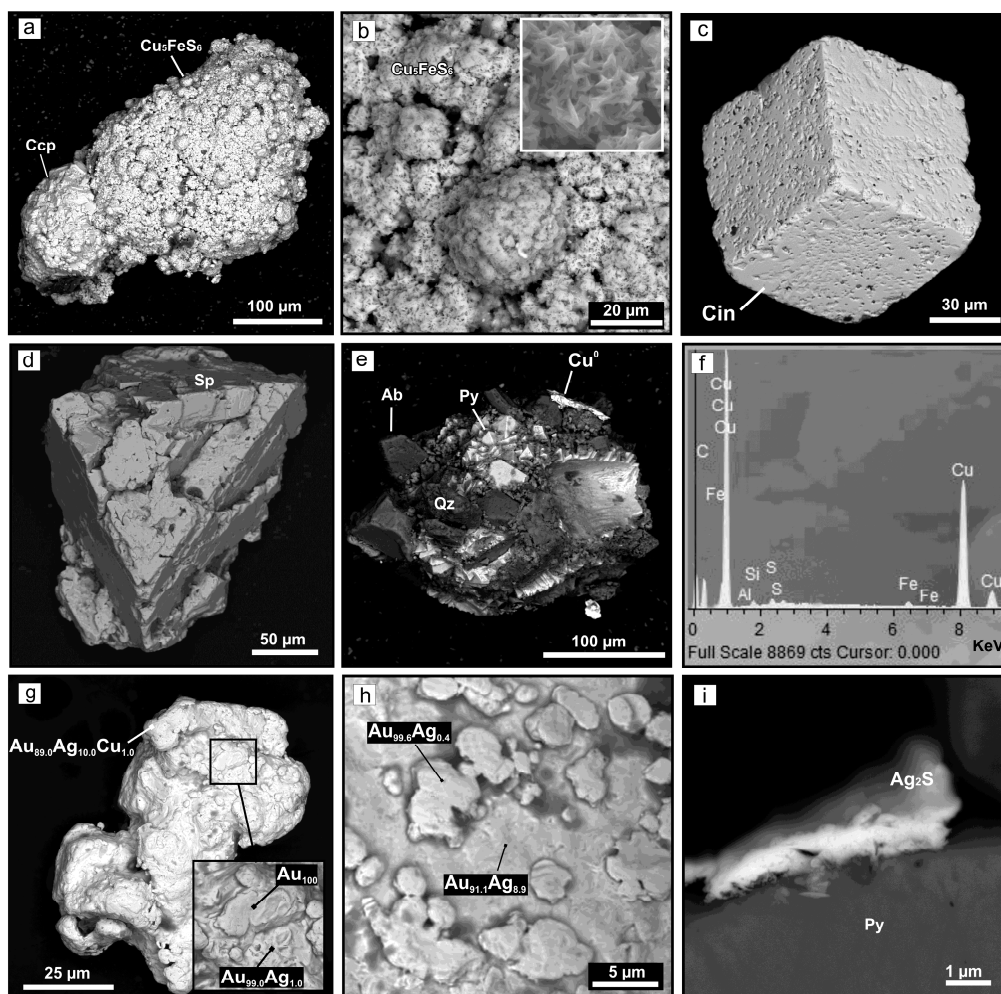


**Figure 12.** Morphology of copper sulphides, cinnabar, sphalerite, silver sulphide and native elements from mud masses (Bulganak area). (a,b) Intergrowth of chalcopyrite and Cu–Fe-sulphide (close to Cu<sub>5</sub>FeS<sub>6</sub>-stoichiometry). Chalcopyrite forms tetrahedrons. Cu<sub>5</sub>FeS<sub>6</sub> occurs as reniform aggregate consisting of numerous star-like microliths with orthorhombic (?) symmetry (b); (c) Euhedral crystal of cinnabar with sharp edges and vertices; (d) Sphalerite tetrahedron with sharp edges and vertices; (e) Thin plate of copper coexisting with pyrite, Fe-(oxy)hydroxides, quartz and detrital albite; (f) EDS spectrum of copper; (g,h) An irregular particles of Au–Ag alloy decorated by later pancake-like overgrowths of gold; (i) Aggregate of silver sulphide (Ag<sub>2</sub>S) coating a pyrite crystal. (a–e,g–i) BSE images. Ab = albite; Ccp = chalcopyrite; Cin = cinnabar; Cu<sup>0</sup> = copper; Sp = sphalerite; Qz = quartz. (a–c,e,g,h) = Tischenko Hill; (d,i) = Andrusov Hill.

Framboids are mostly spherical with diameters from 5 to 50  $\mu\text{m}$  (10–20  $\mu\text{m}$  on average) and consist of spherical, cubic, cubic-octahedral, or more rarely octahedral crystallites, with sizes from 0.5 to 3  $\mu\text{m}$  (Figure 7), arranged most often in an ordered way (sometimes with shared orientations) and rarely with distinct pentagonal or trigonal symmetry (Figure 7b). Some famboids are composed of randomly aggregated crystals. Most of famboids contain intergrown crystallites (filled), while some are open and composed of discrete particles. The space between famboids (both primary and recrystallised) is frequently filled with matrix material (Figure 7b,c).

Framboids show all stages of recrystallisation, propagating commonly from rim to core and ending with the formation of spherules (Figure 7d) which become progressively more euhedral until they evolve into octahedral and cubic-octahedral crystals (Figure 7e,f). The cores of famboids preserve crystallites which are separated by holes and/or are rimmed by massive aggregates of agglomerated particles. Framboids formed at the next stage are completely filled spherules (2–30  $\mu\text{m}$  in diameter); the final stage produces compact aggregates of 3–10- $\mu\text{m}$  isometric particles or euhedral crystals (Figure 7d–h). There are also so-called sunflower structures with famboidal cores rimmed by radiating outer microcrystals (Figure 7c).

Recrystallised pyrite occurs as octahedral, cubic-octahedral or rarely cubic crystals (up to 100–200  $\mu\text{m}$  in size) and their intergrowths (Figure 8). Larger crystals commonly have sculptured surfaces, heavily etched faces and corners, and are dusted with fine cubic or cubic-octahedral microcrystals of later generations. The morphological diversity of authigenic pyrite leaves no doubt about several episodes of nucleation and growth during sedimentation and sediment maturation. Generally, all studied pyrites have textures indicative of early diagenetic process [81].

#### 4.3.3. $\text{FeS}_2$ : Main and Trace Element Composition and Isotopy

The concentrations of main and some trace elements were determined by the EMPA method at the  $\text{FeS}_2$  grain sites free from inclusions. The S/Fe ratio (1.97–1.98) in the famboid crystallites fits the  $\text{FeS}_2$  stoichiometry. They contain up to 0.91 wt % of Mn. The matrix also has the S/Fe ratio  $\sim 2$  but has a deficit of totals (1.3–3.0 wt %) and contains up to 2.19 wt % Mn. Pyrite crystals with the S/Fe ratio about 1.99 host up to 1.33 wt % Mn. EMPA analyses also reveal patchy distribution of Mn, As (up to 0.60 wt %), Cu, Co, and Ni (up to 0.14 wt %, 0.10 wt % and 0.16 wt %, respectively) in pyrite. Marcasite corresponds to the  $\text{FeS}_2$  stoichiometry (S/Fe = 1.98–1.99) and contains up to 0.88 wt % Mn and 0.31 wt % Cu.

Trace element (TE) contents were estimated by ICP-MS in hand-picked concentrates of early pyrite (famboids and pseudomorphs after fossil remnants) and later crystals. The contents of Hg were measured by flameless AAS, in separate aliquots (Table 6). The contents of Zn, Cu, V, Ni and Ag in replica samples may differ by a factor of 1.5–2, possibly, because of the “nugget effect”, which reveals microinclusions of the respective minerals [81–83]. It is more correct and spectacular to compare the TE contents in the pyrite concentrates, which all contain clayey inclusions, as expressed via the relative enrichment factor:  $\text{EF}_{\text{element}} = ([\text{C}]_{\text{element}}/[\text{C}]_{\text{Al}})_{\text{sample}} / ([\text{C}]_{\text{element}}/[\text{C}]_{\text{Al}})_{\text{lithogenic}}$  [45]. In our case, the TE contents were normalised to those of Ga ( $\text{EF}_{\text{element}} = [\text{C}]_{\text{element}}/[\text{C}]_{\text{Ga}}_{\text{sample}} / ([\text{C}]_{\text{element}}/[\text{C}]_{\text{Ga}})_{\text{PAAS}}$ ), which is a close geochemical equivalent of Al [84]. The EF distribution spectra of all pyrite fractions are similar (Figure 13), with three peaks separated by minimums in Zn and Cd: peak I in Mn, Co, Ni, Cu (flat,  $\text{EF} = 10^2\text{--}10^3$ ); peak II in As, Mo, Hg (sharp,  $\text{EF} = 10^3\text{--}10^4$ ); peak III in Sb, Au, Pb (bell-shaped,  $\text{EF} = 10^2\text{--}10^4$ ). The Cd minimum is prominent in all fractions, while that of Zn is more diffuse as Zn contents are quite high in the Andrusov Hill concentrates where sphalerite exists as crystals or possibly as micro-inclusions in pyrite.

**Table 6.** Trace element contents in pyrite fractions from mud masses, Bulganak MV area, Kerch-Taman MV province. ICP-MS data, ppm.

| Location | Andrusov Hill |                                    |                   | Trubetskoy Hill |                   | Tischenko Hill |                   |
|----------|---------------|------------------------------------|-------------------|-----------------|-------------------|----------------|-------------------|
|          | Framboids     | Pseudomorphs after Fossil Remnants | Euhedral Crystals | Framboids       | Euhedral Crystals | Framboids      | Euhedral Crystals |
| Ti       | 27.3          | 471                                | 2.63              | 1.22            | 1.68              | 3.53           | 8.20              |
| Mn       | 4971          | 2529                               | 585               | 2173            | 1465              | 3144           | 1605              |
| Co       | 182           | 145                                | 18.7              | 134             | 32.0              | 130            | 71.0              |
| Ni       | 445           | 386                                | 46.0              | 240             | 63.0              | 325            | 120               |
| Cu       | 797           | 412                                | 70.0              | 358             | 62.0              | 179            | 90.0              |
| Zn       | 965           | 57.0                               | 197               | 56.0            | 25.0              | 83.0           | 46.0              |
| As       | 1148          | 1001                               | 134               | 331             | 175               | 761            | 329               |
| Hg       | 4.20          | 1.25                               | 7.50              | 1.30            | 2.50              | 1.65           | 2.40              |
| Mo       | 111           | 105                                | 17.5              | 22.1            | 18.5              | 70.0           | 19.4              |
| Cd       | 0.61          | 0.5                                | 0.09              | 0.26            | 0.17              | 0.32           | 0.15              |
| Sb       | 17.6          | 43.0                               | 2.32              | 5.00            | 2.13              | 18.2           | 4.23              |
| Au *     | 0.08          | 0.08                               | 0.01              | 0.06            | 0.02              | 0.05           | 0.02              |
| Pb       | 402           | 337                                | 47.0              | 140             | 46.0              | 309            | 78.0              |
| Ga       | 0.53          | 0.10                               | 0.13              | 0.28            | 0.19              | 0.32           | 0.18              |
| V        | 7.18          | 8.08                               | 0.91              | 2.67            | 1.65              | 4.32           | 2.04              |
| Cr       | 12.6          | 9.58                               | 1.85              | 10.1            | 3.18              | 3.47           | 1.29              |

\* the contents of Au were not determined in the bulk sediment sample.

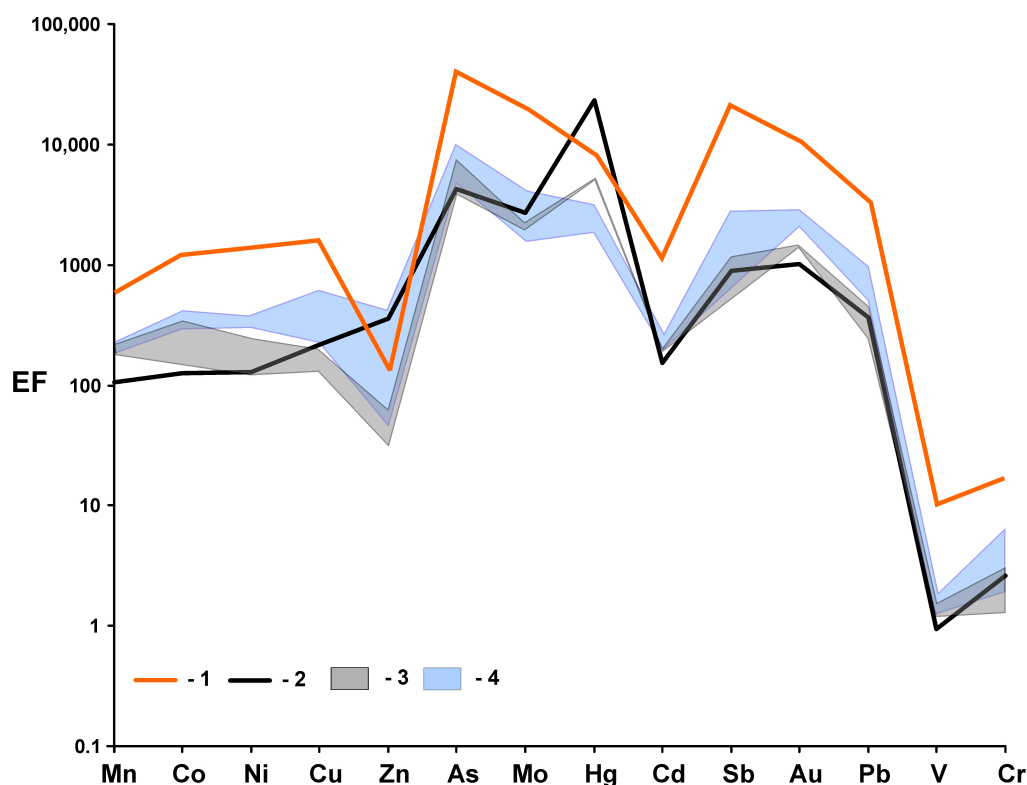


**Figure 13.** Trace element enrichment of framboidal pyrite and pyrite pseudomorphs after fossil remnants versus large euhedral pyrite crystals. ICP-MS data for bulk fractions (Table 6). Relative enrichment factor  $EF_{element} = ([C]_{element}/[C]_{Ga})_{sample}/([C]_{element}/[C]_{Ga})_{PAAS}$  [45]. PAAS after [75]. 1 = pyrite pseudomorphs after fossil remnants (Andrusov Hill); 2 = large euhedral pyrite crystals (Andrusov Hill); 3 = large euhedral pyrite crystals (Trubetskoy and Tischenko Hills); 4 = framboidal pyrite (Andrusov, Trubetskoy and Tischenko Hills).

The EF patterns of framboidal pyrite from different samples are very similar to one another and are generally the same, though at a lower level of values, for the later-generation crystals. The highest EF values correspond to the concentrate of framboids after fossil remnants. Note also that this is the only pyrite fraction with order V enrichment. The abnormal  $EF_{Hg}$  values for the concentrate of pyrite crystals from Andrusov Hill may be due to the presence of cinnabar microinclusions. The difference in TE compositions of early and later pyrite generations is minor for As, Mo, Sb but is much greater for Co, Ni, Cu, Au, and Pb (Figure 13).

TE contents in pyrite and marcasite were determined by LA-ICPMS (Tables 7 and 8), which confirmed regular presence of clayey matter enclosed in framboidal pyrite, as well as in crystals with voids and abrupt growth layers. The EF patterns were plotted for average TE (Figure 14) normalised to the Al content which was determined at each point ( $EF_{element} = ([C]_{element}/[C]_{Al})_{sample}/([C]_{element}/[C]_{Al})_{lithogenic}$ ) [45]. Their shapes changed slightly relative to the bulk fraction spectra (Figures 13 and 14) because LA-ICPMS determined additionally Se, Ag, Sn, Re, Tl, and Bi but did not uncover Hg. Nevertheless, framboidal pyrites from Andrusov and Tischenko Hills preserve the shapes of their EF patterns, with Mn, Co, Ni, and Cu enrichment in framboids, all about  $EF = 10^3-10^4$  (peak I); high enrichment in As, Se, and Mo in both framboids ( $EF = 10^4-10^5$ ) and crystals ( $EF$  to  $10^3-10^4$ ), peak II; Re enrichment ( $EF_{Re} \sim 10^4-10^5$  in framboids and  $EF_{Re} \sim 10^3-10^4$  in crystals) forms peak III. The Zn minimum is distinct in all analysed samples ( $EF \sim 10^1-10^3$ ). Figure 14 clearly shows that pyrite framboids lose all impurity types when recrystallise to crystals in the Andrusov and Tischenko samples, with the greatest decrease in Mn, Cu, Zn, Ag, and Au (two or three orders of magnitude). Unlike these, the crystals and the framboids from Trubetskoy Hill contain similar concentrations of most TE (Mn, Co, Ni, Cu, As, Mo, Cd, and Tl), and the crystals are enriched in Zn, Se, and Au. We attribute this effect to uptake of foreign inorganic particles by rapidly growing defect crystals which are abundant in the sample (Figure 8b).

**Table 7.** Trace element composition of pyrite framboids from mud masses, Bulganak MV area, Kerch-Taman MV province. LA-ICPMS data, ppm.

| Location | Andrusov Hill |       |       | Trubetskoy Hill |       |       | Tischenko Hill |       |      |
|----------|---------------|-------|-------|-----------------|-------|-------|----------------|-------|------|
|          | Mean (n = 23) | Min   | Max   | Mean (n = 12)   | Min   | Max   | Mean (n = 16)  | Min   | Max  |
| Al       | 32.8          | 0.20  | 271   | 91.9            | 18.8  | 231   | 98.0           | 0.96  | 248  |
| Ti       | 2.80          | 0.27  | 14.7  | 11.9            | 1.72  | 37.8  | 6.97           | 0.44  | 34.7 |
| Mn       | 1209          | 67.7  | 3654  | 958             | 78.5  | 2323  | 1853           | 351   | 5715 |
| Co       | 79.3          | 0.23  | 355   | 141             | 0.8   | 345   | 46.1           | 1.03  | 206  |
| Ni       | 116           | 5.76  | 438   | 383             | 1.61  | 714   | 140            | 2.98  | 392  |
| Cu       | 123           | 1.34  | 1004  | 842             | 23.9  | 1656  | 203            | 6.23  | 678  |
| Zn       | 30.3          | 2.18  | 87.9  | 18.9            | 6.96  | 33.1  | 32.2           | 6.25  | 60.1 |
| As       | 248           | 3.74  | 1466  | 164             | 6.84  | 262   | 148            | 12.1  | 526  |
| Se       | 7.67          | 0.85  | 22.3  | 11.7            | 3.63  | 26.8  | 10.1           | 1.91  | 37.8 |
| Zr       | 0.42          | 0.11  | 1.79  | 0.57            | 0.33  | 1.06  | 0.93           | 0.08  | 2.81 |
| Mo       | 6.55          | 0.08  | 35.3  | 3.67            | 0.33  | 8.91  | 10.7           | 0.15  | 48.4 |
| Ag       | 0.43          | 0.01  | 3.19  | 2.19            | 0.61  | 3.93  | 0.82           | 0.02  | 3.24 |
| Cd       | 0.08          | 0.01  | 0.39  | 0.17            | 0.12  | 0.21  | 0.13           | 0.01  | 0.33 |
| Sn       | 0.34          | 0.13  | 1.06  | 6.59            | 0.19  | 25.2  | 0.28           | 0.13  | 0.44 |
| Sb       | 1.44          | 0.06  | 2.82  | 2.28            | 1.12  | 3.94  | 2.72           | 0.13  | 6.75 |
| Te       | 0.46          | 0.05  | 1.37  | 0.58            | 0.48  | 0.68  | 0.89           | 0.12  | 2.33 |
| Ce       | 0.12          | 0.002 | 0.45  | 0.17            | 0.02  | 0.26  | 0.25           | 0.01  | 0.93 |
| Re       | 0.04          | 0.002 | 0.11  | 0.005           | 0.002 | 0.007 | 0.02           | 0.001 | 0.05 |
| Au       | 0.02          | 0.004 | 0.06  | 0.02            | 0.01  | 0.05  | 0.02           | 0.01  | 0.03 |
| Tl       | 3.70          | 0.27  | 14.1  | 2.69            | 1.28  | 5.15  | 1.34           | 0.11  | 3.42 |
| Pb       | 47.8          | 0.12  | 511.6 | 250             | 2.68  | 664   | 68.9           | 2.63  | 207  |
| Bi       | 0.24          | 0.004 | 2.84  | 1.72            | 0.83  | 3.45  | 0.23           | 0.01  | 0.42 |
| Re/Mo    | 0.006         |       |       | 0.001           |       |       | 0.002          |       |      |
| Te/Se    | 0.06          |       |       | 0.05            |       |       | 0.09           |       |      |
| Sb/Se    | 0.19          |       |       | 0.19            |       |       | 0.27           |       |      |
| Tl/Se    | 0.48          |       |       | 0.23            |       |       | 0.13           |       |      |

n = number of analyses.

**Table 8.** Trace element composition of pyrite and marcasite crystals from mud masses, Bulganak MV area, Kerch-Taman MV province. LA-ICPMS data, ppm.

| Location | Tischenko Hill   |       |      | Andrusov Hill    |       |       |                  |       |       | Trubetskoy Hill  |       |       |
|----------|------------------|-------|------|------------------|-------|-------|------------------|-------|-------|------------------|-------|-------|
| Ineral   | Pyrite           |       |      | Pyrite           |       |       | Marcasite        |       |       | Pyrite           |       |       |
| Element  | Mean<br>(n = 11) | Min   | Max  | Mean<br>(n = 13) | Min   | Max   | Mean<br>(n = 10) | Min   | Max   | Mean<br>(n = 10) | Min   | Max   |
| Al       | 760              | 2.7   | 2029 | 62.6             | 25.5  | 91.1  | 214              | 10.8  | 777   | 35.0             | 0.40  | 99.1  |
| Ti       | 86.5             | 2.7   | 257  | 10.2             | 1.95  | 17.9  | 25.7             | 4.68  | 38.5  | 8.22             | 0.39  | 32.7  |
| Mn       | 2012             | 12.3  | 6208 | 13.1             | 0.67  | 64.8  | 72.5             | 1.93  | 215   | 215              | 3.93  | 434   |
| Co       | 8.69             | 1.81  | 86.4 | 6.15             | 0.25  | 28.5  | 10.3             | 0.59  | 20.0  | 3.11             | 1.57  | 7.87  |
| Ni       | 14.2             | 4.52  | 271  | 42.8             | 0.84  | 176   | 15.5             | 1.07  | 36.8  | 8.70             | 2.60  | 18.6  |
| Cu       | 112              | 3.19  | 647  | 16.7             | 0.93  | 32.5  | 1.86             | 0.81  | 2.91  | 39.2             | 1.68  | 82.2  |
| Zn       | 76.9             | 1.62  | 296  | 8.16             | 0.51  | 26.7  | 6.29             | 0.66  | 14.8  | 17.2             | 1.21  | 41.1  |
| As       | 490              | 3.10  | 933  | 1034             | 0.33  | 2104  | 278              | 0.23  | 865   | 23.1             | 2.71  | 60.3  |
| Se       | 13.4             | 4.15  | 46.1 | 10.2             | 3.30  | 18.2  | 46.5             | 46.5  | 46.5  | 9.42             | 1.51  | 17.5  |
| Zr       | 6.12             | 0.16  | 23.9 | 0.17             | 0.07  | 0.36  | 0.63             | 0.03  | 1.62  | 0.14             | 0.04  | 0.29  |
| Mo       | 45.4             | 0.35  | 121  | 204              | 0.03  | 539   | 15.5             | 0.02  | 61.3  | 7.56             | 0.34  | 18.5  |
| Ag       | 2.80             | 0.03  | 10.3 | 0.10             | <0.02 | 0.12  | 0.07             | <0.02 | 0.09  | 0.10             | 0.03  | 0.16  |
| Cd       | 0.29             | 0.01  | 0.45 | 0.10             | 0.04  | 0.22  | 0.03             | 0.01  | 0.05  | 0.02             | <0.01 | 0.03  |
| Sn       | 0.35             | 0.21  | 0.48 | 0.23             | 0.20  | 0.25  | 0.20             | <0.12 | 0.24  | 0.28             | 0.20  | 0.39  |
| Sb       | 13.1             | 0.27  | 54.0 | 22.3             | 1.46  | 49.0  | 1.74             | 0.02  | 6.41  | 1.41             | 0.20  | 2.77  |
| Te       | 6.65             | 1.93  | 6.87 | <0.04            | <0.04 | <0.04 | <0.04            | <0.04 | <0.04 | 0.02             | <0.01 | 0.08  |
| Ce       | 0.92             | 0.01  | 3.25 | 0.06             | 0.02  | 0.15  | 0.36             | 0.02  | 0.99  | 0.04             | 0.01  | 0.07  |
| Re       | 0.01             | 0.004 | 0.05 | 0.004            | 0.001 | 0.007 | <0.01            | <0.01 | <0.01 | <0.01            | <0.01 | <0.01 |
| Au       | 0.02             | 0.01  | 0.03 | 0.007            | 0.003 | 0.02  | 0.01             | 0.004 | 0.01  | 0.01             | 0.01  | 0.01  |
| Tl       | 1.21             | 0.01  | 2.37 | 2.64             | 0.05  | 5.22  | 1.31             | 0.04  | 4.70  | 3.17             | 0.67  | 6.4   |
| Pb       | 249              | 2.46  | 1083 | 11.5             | 0.22  | 54.60 | 2.37             | 0.40  | 7.37  | 2.11             | 0.40  | 5.06  |
| Bi       | 0.25             | 0.01  | 1.06 | 0.17             | 0.02  | 0.32  | 0.01             | 0.004 | 0.01  | 0.01             | 0.004 | 0.038 |

n = number of analyses.

The TE composition of marcasite was studied only in the Andrusov Hill sample where the mineral is relatively common. The pyrite and marcasite crystals have similar EF patterns but the latter are markedly depleted in Mo and Re (Table 8) and have a high value of  $EF_{Ag} \sim 10^3$  (Figure 14).

All analysed pyrites show  $^{34}S$  depletion relative to seawater sulphate (about +20‰) [42] (Figure 15). The  $\delta^{34}S_{pyrite}$  compositions are the lightest in the Tischenko samples (+0.4‰ and −1.5‰ for framboids and +0.4‰ for crystals), the heaviest in Andrusov Hill (+8.9‰ and +8.2‰, respectively), and intermediate in Trubetskoy Hill (+5.7‰ and +7.4‰ for framboids and +4.0‰ for crystals).

#### 4.3.4. Host Minerals for Hg, Zn, Cu, Pb, Ag, Au

Cinnabar, sphalerite and akantite were found in the sulphide concentrate from Andrusov Hill, whereas Cu–Fe and Pb sulphides, native Cu, Au and (Au, Ag) alloys were found in Tischenko Hill (Figure 12).

Cinnabar mainly occurs as massive aggregates of anhedral micrograins with trigonal etch pits; less often it forms subhedral grains with sharp edges and corners and even perfect crystals with pinacoidal and rhombohedral faces (Figure 12c). Cinnabar corresponds to the  $Hg_{0.97}S_{1.03}$  composition (85.42–85.68 wt % Hg and 14.41–14.87 wt % S) with patchy distributions of Cu (1.05 wt %), Fe (0.94 wt %), and Zn (up to 0.38 wt %), which may indicate the presence of finest inclusions of the respective sulphides.

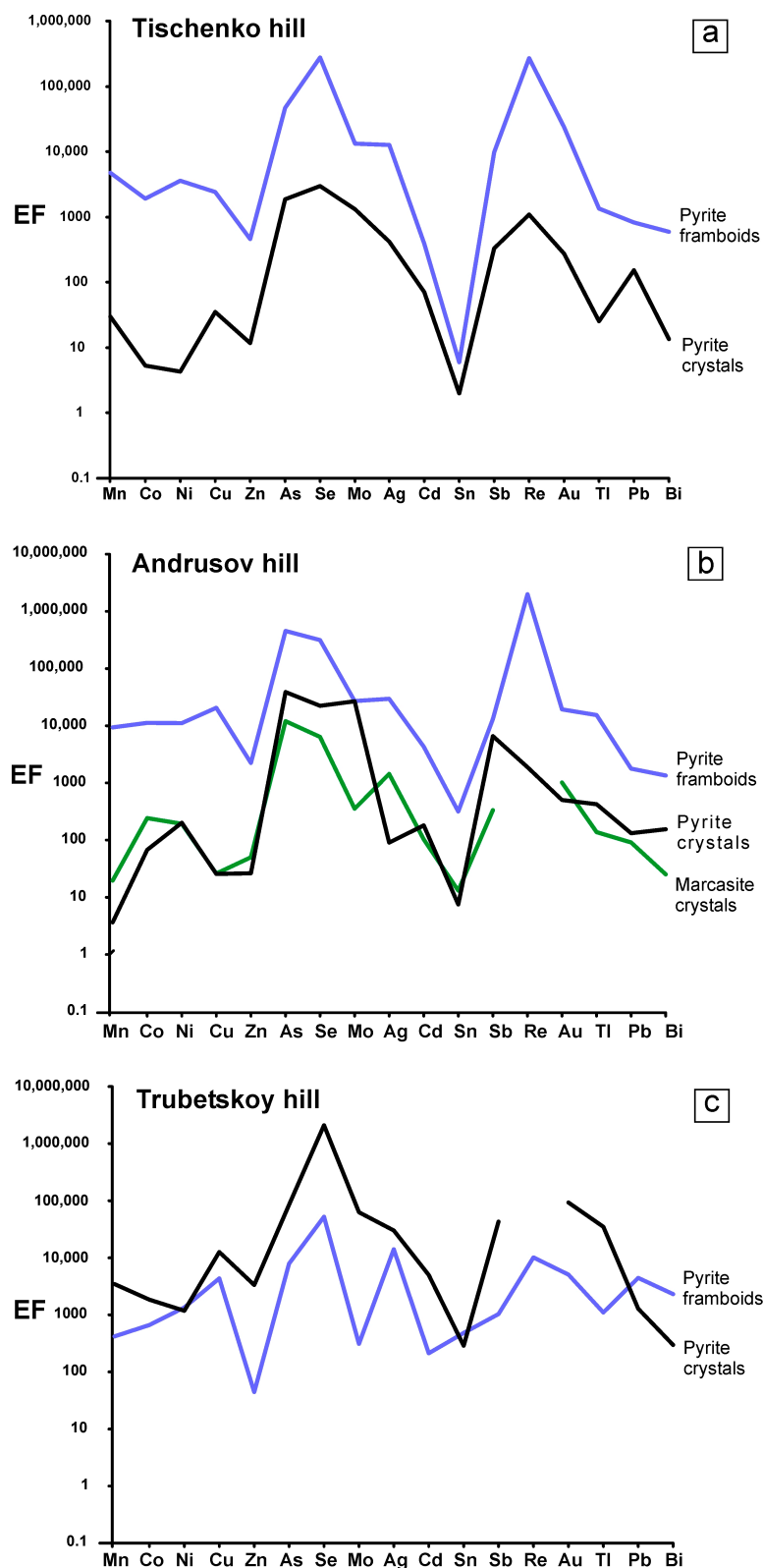


**Figure 14.** Incorporation of trace elements in different textural forms and polymorphic modifications of FeS<sub>2</sub>. LA-ICPMS analyses of pyrite and marcasite (Tables 7 and 8). Relative enrichment factor:  $EF_{\text{element}} = ([C]_{\text{element}}/[C]_{\text{Al}})_{\text{sample}} / ([C]_{\text{element}}/[C]_{\text{Al}})_{\text{PAAS}}$  [45]. PAAS after [75]. (a) Tischenko hill, (b) Andrusov hill, (c) Trubetskoy hill.

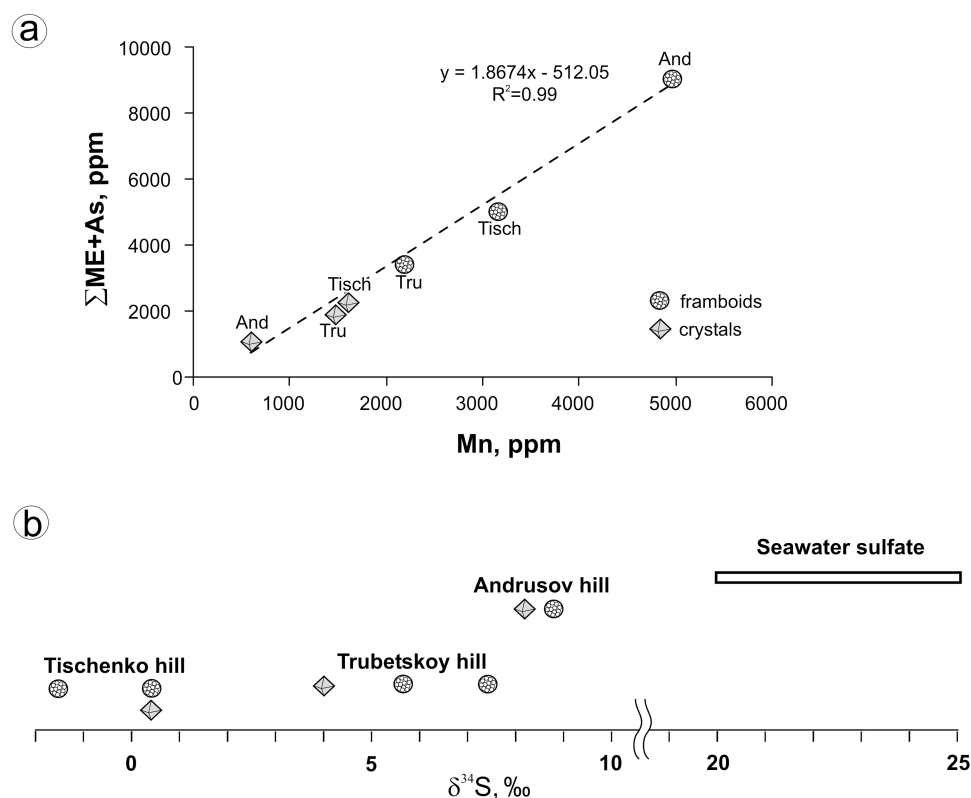


**Figure 15.** Trace element loading (a) and stable sulphur isotope composition (b) of pyrite from the MMS. ME = V + Cr + Mn + Co + Ni + Cu + Zn + Mo + Cd + Sb + Au + Pb. Sulphur isotope composition of sea water sulfate after [42].

Sphalerite occurs as straw yellow tetrahedrons, up to 200  $\mu\text{m}$  in size (Figure 12d), and has sharp edges and corners and complex microtopography of face surfaces with numerous abrupt growth layers. The mineral contains Zn (65.42–65.84 wt %), Fe (0.34–0.55 wt %) and S (32.71–33.15 wt %) corresponding to the formula  $\text{Zn}_{0.97}\text{Fe}_{0.01}\text{S}_{1.00}$ . Other TE concentrations (Cd, Cu, As, Sb) are below the EMPA detection limits.

Cu–Fe sulphides (chalcopyrite and nukundamite) were found intergrown (Figure 12a,b). Chalcopyrite occurs as 5–20  $\mu\text{m}$  tetrahedrons. The EMPA data (29.80 wt % Fe, 33.47 wt % Cu, 34.81 wt % S and 1.17 wt % As) lead to the formula  $\text{Cu}_{0.98}\text{Fe}_{0.99}\text{S}_{2.01}\text{As}_{0.03}$ . Another Cu–Fe sulphide exists as reniform aggregates (with spheroids 10–25  $\mu\text{m}$  in diameter) consisting of numerous 1–2  $\mu\text{m}$  stellar microcrystals (twins or skeletal forms?). Its composition (56.18–56.64 wt % Cu, 8.56–8.90 wt % Fe, and 34.26–34.23 wt % S;  $\text{Cu}_{5.04}\text{Fe}_{0.89}\text{S}_{6.07}$ ) corresponds to nukundamite ( $\text{Cu}_5\text{FeS}_6$ ) [85,86].

Akantite ( $\alpha\text{-Ag}_2\text{S}$ ) was found only once as flakes on the pyrite crystals surface (Figure 12i).

Pb Sulphide was found as a single tiny ( $\sim 1\ \mu\text{m}$ ) particle hosted by a fine-grained aggregate with Fe-rich carbonate, gypsum and Fe-(oxy)hydroxides.

Gold and gold-silver alloys mainly occur as massive, lumpy, or flattened 30–150  $\mu\text{m}$  particles (60–80  $\mu\text{m}$  in average). Gold particles bear neither signatures of wear and long distance transport, nor etch grooves and pits which would indicate dissolution under supergene conditions. The surfaces of a few gold particles are decorated with later pancake-like overgrowths. They vary in fineness from 736 to 1000, higher in the rims ( $\sim 890$ – $990$ ) and in the pancake-like overgrowths ( $\sim 995$ ). The cores are richer in Ag ( $\sim 800$ – $950$ ) (Figure 12g,h), but traces of copper (0.6–1.0 wt %) are restricted to the rims.

Metallic copper occurring as thin ( $\sim 10\ \mu\text{m}$ ) foil was found aggregated with quartz, albite, and pyrite crystals (Figure 12e,f).

## 5. Discussion

### 5.1. Provenance of the Middle Maykopian Sedimentation in the Western Termination of the Indol-Kuban Trough: Mineralogical Evidence

The mineralogy and abundance of clastic (including HM) and clay minerals have implications for the provenance, deposition environments, weathering, diagenesis, and palaeogeography. The MMs from the Bulganak MV field are mainly composed of sandy illite clay with relatively high kaolinite and low mix illite-smectite percentages, which records diagenetic alteration of primary mud in a buried zone. More rigorous constraints on the burial depth based on illite/smectite ratios are beyond the scope of this paper, but we will discuss the potentiality and limitations of illite-smectite thermometry.

The illite/smectite ratio and the vitrinite reflectance ( $R_0$ ) are useful indicators of sediment maturation degree as both are irreversible and record the maximum temperature ever attained by the rocks. These parameters allow plotting temperature variations for specific basins when used jointly [87,88], but the illite/smectite ratios alone cannot provide precise thermometric constraints. Although there exist numerous thermodynamic models and data characterising low-temperature phyllosilicates, as well as experimental constraints on their phase-temperature relationships, no direct reaction bracketing is available, because the kinetics of illite-to-smectite transition is too sluggish below 200 °C [89]. As shown by detailed mineralogical and experimental studies, illite-to-smectite transition is not a simple dehydration reaction mainly controlled by equilibrium but a complex process involving progressive conversion of smectite to illite accompanied by change of Si:Al:K stoichiometry [89] or Fe reduction at octahedral sites leading to increased layer charge, coupled with K fixation [90]. The K-rich pore fluid in shales tends to buffer illite within its stability field, and illitisation can be treated as a kinetic process mostly occurring in the temperature range from 70 to 130 °C [89,91]. The conversion proceeds via increase in illite contents in mix illite-smectite from ~20% to ~80%, and is the fastest between 90 and 120 °C [91]. The mix illite-smectite phases in all analysed Bulganak MM samples contain about 70% of illite layers, i.e., the primary marine sediments experienced diagenetic alteration at 80 to 100 °C. These estimates are consistent with fluid generation temperatures ( $T_{Mg/Li}$ ) from 76 to 117 °C and suggest the presence of a mud reservoir at a depth of 2.5–3.5 km. The Bulganak MVs extrude fluidised mature shales mobilised from the lower Middle Maykop section. The expelled aqueous fluids are mature pore waters that formed when saline sea water buried together with primary smectite-dominated mud mixed up with fresher B- and Li-rich waters released by smectite dehydration.

High contents of kaolinite and low percentages of non-resistant minerals (chlorite, muscovite, epidote and amphibole) in the MM and Middle Maykop Shale samples indicate that clastic inputs to the western termination of the Indol-Kuban Trough were mostly from mature kaolinite weathering profiles in the Russian Platform [52]. All HM ultrastable assemblages consist of abundant rutile, ilmenite, sillimanite, kyanite, ( $\pm$ andalusite), and garnet with minor tourmaline, zircon, titanite, and apatite. They comprise diverse index phases mainly derived from peraluminous high-grade metamorphic and granitic rocks and represent clastic inputs from the Ukrainian shield. The roundness of ultrastable HM grains indicates distant clastic transportation by large river systems (paleo-Don, paleo-Kuban, etc.) [52,54,55]. The Caucasian mountain system was the provenance for assemblages of scarce non-resistant minerals (epidote, pyroxene, amphibole, and chlorite). Therefore, the contribution of the southern provenance into the western Indol-Kuban Trough was limited during the Middle Maykopian sedimentation. The Middle Maykop Shales contain more non-resistant minerals than the Bulganak MMs because the Taman Peninsula is closer to the Caucasus than the Kerch Peninsula (Figure 1).

## 5.2. Main Trends of Trace Element Sequestration by Mineral Hosts in Oxygen-Deficient Environments

### 5.2.1. Geochemical Fingerprints of Carbonates

Commonly most reactive Fe and Mn enter deep-water marine sediments as a very fine-grained Fe<sup>3+</sup>- and Mn<sup>4+</sup>-(oxy)hydroxides [92], which is also the case for the analysed sediments. During diagenesis in oxygen-deficient environments, Mn<sup>4+</sup>-(oxy)hydroxides underwent early reduction which precedes both Fe<sup>3+</sup> and sulphate reduction and the related production of H<sub>2</sub>S [93,94]. Almost all Mn<sup>2+</sup> reduced from Mn<sup>4+</sup> and Mn<sup>3+</sup> enters the pore solution and then precipitates as carbonates [41,77,92], while a considerable part of iron still remains in Fe<sup>3+</sup>-(oxy)hydroxides and Fe<sup>3+</sup>-bearing layered silicates. Indeed, all studied MM samples contain Fe-(oxy)hydroxides, illite and glauconite, are free from Mn-(oxy)hydroxides, but contain diverse Mn-bearing carbonates (Figure 10; Table 3).

The members of the MnCO<sub>3</sub>–CaCO<sub>3</sub>, CaMn(CO<sub>3</sub>)<sub>2</sub>–CaMg(CO<sub>3</sub>)<sub>2</sub>, and FeCO<sub>3</sub>–MnCO<sub>3</sub> series were previously recognised as the major sink of Mn<sup>2+</sup> in anoxic sediments [77,95,96]. Romanek et al. [77] also inferred that metastable mix carbonates may be another significant Mn sink in marine sediments. Our discovery of natural Mn-bearing mix carbonates in the Maykop Shales supports this idea. Under weakly reducing conditions in suboxic but non-sulphidic environments, most Mn is stored in carbonate sinks immediately before the formation of sulphides. As a result, early framboidal pyrite grows from a medium depleted in Mn<sup>2+</sup>.

Since the reduction of Fe<sup>3+</sup> to Fe<sup>2+</sup> requires a higher reducing potential than that of Mn<sup>3+(4+) → Mn<sup>2+</sup> [93,94], it would be reasonable to expect regeneration or overgrowing of early Mn-rich carbonates by later Fe-rich ones. However, we failed to find any zoned carbonate grains with Mn-rich cores and Fe-rich rims, but found persistent coupling of fine-crystalline intergrowths of siderite with Fe-(oxy)hydroxide clots, and only mix carbonates beyond these aggregates. This distribution of numerous fine siderite crystals (Figure 6b) indicates mass nucleation of FeCO<sub>3</sub> and proves that supersaturation with respect to Fe<sup>2+</sup> is restricted to the pore solution volume, namely, to thin films enveloping Fe-(oxy)hydroxides clots.</sup>

Earlier experiments of Romanek et al. [77] in the system FeCO<sub>3</sub>–MgCO<sub>3</sub>–CaCO<sub>3</sub> showed siderite to grow most rapidly among other Fe-bearing carbonates (at T = 25–250 °C). Precipitation of Mg-siderite is indicative of very high Mg/Fe ratios (≥10) in the growth medium, while the incorporation of Mg into the FeCO<sub>3</sub> structure slows down considerably the precipitation kinetics. In the same way, (Fe,Ca)CO<sub>3</sub> carbonates, rather than siderite and calcite, preferably grow from solutions with Ca/Fe molar ratios of 0.03 to 1.11. Precipitation of calcite, in turn, is inhibited by high Mg concentrations in seawater, also leading to the growth of mix carbonates [77]. Thus, Fe<sup>2+</sup> concentration in pore water decreased while the contents of main seawater cations (Mg and Ca) increased in immature sediments away from the primary storages of highly-reactive iron, which retarded the siderite nucleation and led to the growth of larger crystals of Mg-siderite and other mix carbonates. Temperature is another key control of their compositions: as the temperature falls from 70 °C to 25 °C, Mg–Ca siderite, instead of Ca–Fe magnesite, precipitates from Fe<sup>2+</sup>-, Mg<sup>2+</sup>-, and Ca<sup>2+</sup>-bearing solutions supersaturated with respect to magnesite (Ω<sub>mag</sub> = 170) [77].

Thus, mix carbonates formed during early diagenesis of the Middle Maykop shales under control of several factors: (1) availability of highly-reactive (mainly amorphous) Fe(Mn)-(oxy)hydroxides; (2) seawater composition with Mg strongly exceeding the concentrations of other cations [97]; (3) suboxic or weakly reducing conditions, optimal for outpacing reduction of Mn<sup>4+</sup> and restricted reduction of Fe<sup>3+</sup>; (4) low temperatures (of about 8 °C) of bottom water and subbottom mud. The joint action of these (mainly kinetic) factors made mix cation carbonates (along with siderite) the principle Fe sinks in oxygen-deficient (or weakly sulphidic) environments.

Both bulk Fe-rich fractions of authigenic carbonates and their individual crystals showed Zn enrichment (up to 0.2 wt % ZnO). Possible mechanisms of Zn and Cd accumulation in marine carbonates have been discussed in our recent publication [47]. According to the model of Zn co-precipitation with CaCO<sub>3</sub> [98], zinc appears to remain on the calcite surface as hydrated complexes

or as  $Zn_5(OH)_6(CO_3)_2$  (hydrozincite) films, which may incorporate into calcite by recrystallisation due to low solubility of hydrozincite ( $K_{sp} = 10^{-14.9}$  at 25 °C) [99]. Thus, a large part of Zn resided in carbonates early during diagenesis already, under weakly reducing conditions, and thus could not contribute to later precipitation of sulphides triggered by sulphate reduction.

Diagenetic carbonate growth has been unanimously recognised to be a single-event process occurring early during diagenesis. Carbonates grow in sediments at shallow burial depths below the seafloor; they commonly survive themselves and preserve their geochemical fingerprints even in old rocks spared by metamorphism [80,100]. There are three distinct depositional environments that may lead to precipitation of Fe( $\pm$ Mn)-rich carbonates [41,101]: (1) suboxic diagenesis in slowly deposited pelagic sediments with low concentration of organic matter, an optimal environment for siderite precipitation; (2) suboxic Fe(Mn)-(oxy)hydroxide reduction and microbial methanogenesis under unlimited inputs of highly reactive iron, at shallow burial depths below the seafloor, favorable for precipitation of Fe- and Mn-carbonates; (3) reduction of sulphate and  $Fe^{3+}$  (at a rate that balances or exceeds the sulphate reduction rate), which can maintain co-precipitation of Fe-rich carbonates and Fe sulphides, if reactive iron is available.

Abundant Fe(Mn)- and mix carbonates coexisting with relatively scarce  $FeS_2$  in the samples we studied, as well as their concordantly changing trace element and isotopic patterns, suggest a syngenetic origin early during diagenesis of the Middle Maykop shales, by scenario (3). Depletion of the analysed authigenic carbonates in both  $^{12}C$  and  $^{16}O$  relative to their marine counterparts from the zone of active sulphate reduction and microbial methanogenesis [41] points to a mineral-forming medium rich in  $(SO_4)^{2-}$ , at lower organic carbon contents in the sediment, and inhibited sulphate-reducing activity and methanogenesis. Judging by the narrow  $\delta^{13}C$  range ( $\delta^{13}C = +2.1$  to  $+3.7\%$  VPDB), most of carbon in the carbonates came from a single seawater inorganic source ( $\delta^{13}C = -2$  to  $+2\%$  VPDB), without inputs of oxidised organic matter ( $\delta^{13}C \sim -25\%$  VPDB) and/or methane ( $\delta^{13}C_{HCO_3} \sim -75\%$  VPDB) [102]. The enrichment of siderite in  $^{18}O$  relative to the coexisting mix carbonates may also indicate a contribution from an  $^{18}O$ -enriched source, possibly associated with  $^{18}O$ -rich pore water and/or dissociation of gas hydrates [103,104]. An assemblage similar to that we studied (Fe(oxy)hydroxides +  $FeS_2$  + Fe–Mn carbonates + barite-celestine) was recently shown [104] to be a single mineral complex that formed during early diagenesis of marine sediments at decomposition of methane hydrate.

Authigenic carbonates are most often compositionally homogeneous, while zoned, regenerated, and recrystallised Fe–Mn- and mix authigenic marine carbonates are very rare. One such example was described by Chow et al. [41], who suggest that continuous crystal growth, with composition change upon burial, was possible due to high pre-cement porosity of the sediments. Note that authigenic carbonates in the studied MMs do not show aligned/flattened intergrowths and zoned crystals, the structures of overgrowth, regeneration, and/or replacement of earlier carbonates by later generations, or partial dissolution of crystals. Judging by the absence of all these signatures, carbonate precipitation in the sediment in our case was rather a single event that most likely predated compaction. It is most likely kinetic rather than thermodynamic factors that impeded the growth of authigenic carbonates in the Maykop shales. Their individual grains became encapsulated in compact clayey coat, which blocked the exchange processes already during early diagenesis, due to low permeability of shales which progressively increased with depth.

### 5.2.2. Trace Element Composition of Sedimentary $FeS_2$ and TE Partitioning during Diagenesis

TE concentrations in sedimentary pyrite track the primary elemental abundance in coeval seawater. Thus, pyrite of any Cenozoic marine sediment is enriched in the same TE elements as the current oxygenated ocean: Mo, As, Ni, Zn, Cu, Se [81]. Indeed, pyrites in the MMs we studied show Mo, As, Ni, Cu, and Se peaks (Figure 14) and contain the same amounts (>10 up to <100 ppm) of Cd, Sb, Ag, and Tl as pyrite from any other Cenozoic marine sediments [81]. Moreover, the Kerch-Taman authigenic pyrites and current seawater have basically similar TE distribution patterns (Figure 16).

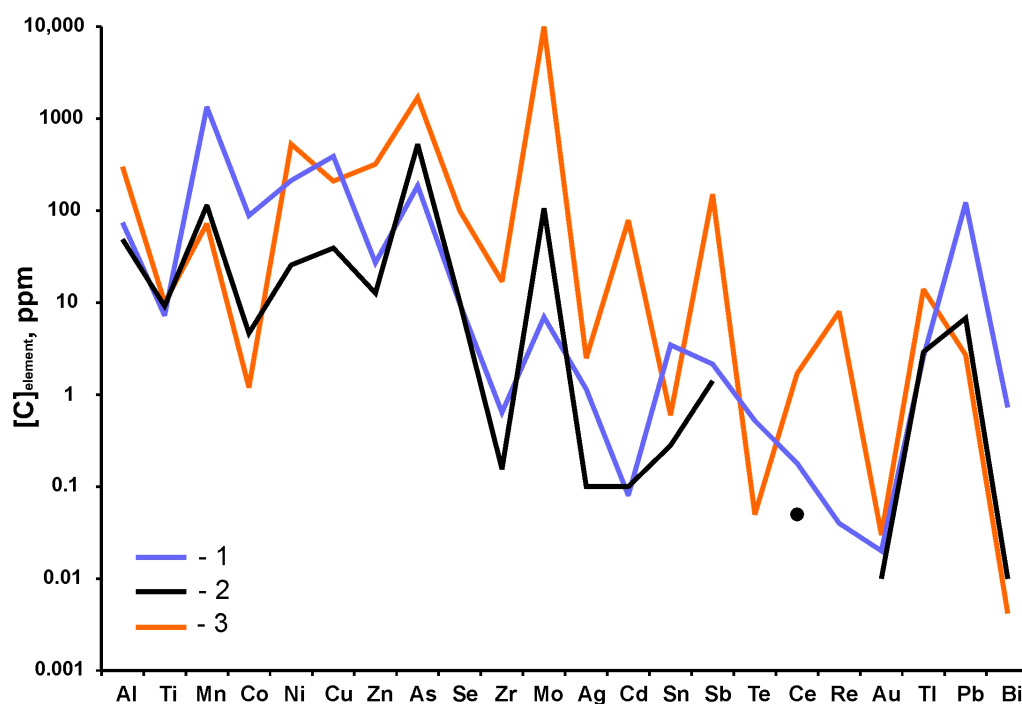


**Figure 16.** Trace element patterns of frambooidal pyrite (1) and pyrite crystals (2) from Bulganak MV area in comparison with sea water (3) [105]. LA-ICPMS data for average composition of pyrites from Andrusov, Trubetskoy and Tischenko Hills (Tables 7 and 8). TE concentration in sea water is  $[C]_{\text{element}} \cdot 10$ .

The analysed pyrites differ from others in Zn and Cd depletion, as well as in Pb, Mn and Re enrichment (Figure 14). Tribouvillard [106] considered pyrite to be the main Zn host in oxygen-deficient sediments and reported zinc incorporation into pyrite by the  $\text{Zn}^{2+} \rightarrow \text{Fe}^{2+}$  substitution. It occurs as ZnS micro-phases or domains which can co-crystallise with  $\text{FeS}_2$  or enter the  $\text{FeS}_2$  matrix during diagenesis. On the other hand, Zn and Cd in immature recent and pre-Quaternary sediments were found to form discrete sulphides rather than being incorporated into pyrite [46,47,107–109]. The presence of sphalerite crystals in MMs is evidence of the latter scenario of Zn behaviour in the formation of the parent sediments. Furthermore, the prominent Zn minimum in the EF patterns of the pyrite crystals, frambooids, and bulk sulphide fractions (Figures 13 and 14) attests to Zn storage by earlier precipitated authigenic solids, namely carbonates.

Low contents of Cd in all our samples are most likely due to low bioproductivity of the Maykop stagnant and freshened basin, because biogenic shuttle of Cd to the marine sediments has been its main source [110,111].

Lead tends to be introduced into marine basin by hydrothermal activity [48]. The water of the Oligocene-Miocene Indol-Kuban basin apparently received Pb from the Greater Caucasus in the south, with numerous Pb–Zn deposits [112].

Manganese enrichment of both carbonates and matrix of earlier frambooidal pyrites can be reasonably explained by the lithology of the provenance that supplied sediments to the western flank of the Indol-Kuban Trough: Oligocene Mn carbonates and their thick eluvium extend, with some gaps, along the southern slope of the Ukraine shield in a 25 km wide and 250 km long zone which accommodates the Europe largest Nikopol Mn deposit [113].

Since highly-reactive Fe-(oxy)hydroxides were obviously in excess during the Maykop deposition, pyrite crystallisation is expected to be limited by local  $[\text{HS}^-]$  concentration. The lower the  $[\text{HS}^-]$  concentrations, the less pyrite could precipitate and the more TE it captured from the pore solution [81]. The highest TE sequestration by earlier frambooids from Andrusov Hill, along with their heaviest

sulphur isotopic composition ( $\delta^{34}\text{S} = +8.9\text{‰}$ ) and highest Re/Mo ratio, suggest depressed biogenic reduction of seawater sulphate during their formation. Other framboids result from prolific microbially mediated sulphate reduction, judging by similar EF patterns, though with lower absolute TE concentrations, as well as by lighter  $\delta^{34}\text{S}$  contents and lower Re/Mo ratios.

While re-crystallising into both pyrite and marcasite crystals, the framboids become depleted in most TE but retain high As and Mo contents (Figure 14). The SEM data leave no doubt that some TE (Cu, Ag, Au, Pb) that released during the recrystallisation of framboidal pyrite became then stored in quite large particles of sulphides, metals or alloys. Other TE may occur as microinclusions in pyrite crystals, as indicated by their “patchy” distributions revealed by both EMPA and LA-ICPMS (Tables 7 and 8). The amount of impurities the framboidal pyrite loses during re-crystallisation varies in different samples (Figure 14) and obviously correlates with the type and diversity of coexisting TE host minerals. This percentage is the highest for the Tischenko Hill pyrites which are mostly depleted in Cu, Au, Ag and Pb. The respective heavy fraction contains three phases of Cu, Au, (Au, Ag) alloys and Pb sulphide (Table 3). The Andrusov Hill pyrites have lost a lower amount of impurities: they are depleted in Ag and Zn, while sphalerite, akantite and cinnabar are present in the sulphide concentrate (Figures 12 and 14; Table 3). The contents of most TE in the pyrite crystals and framboids from the Trubetskoy Hill sample are commensurate, but the crystals have greater Se, Mo and Mn enrichments than the framboids (Figure 14). However, this may be a false effect rather associated with defects and occluded solid inclusions in pyrite crystals (Figure 8). No TE hosts other than  $\text{FeS}_2$  have been found in the sample.

The fate of Zn, Cd, Cu and Hg during the evolution of authigenic sulphides under oxygen-deficient conditions requires separate consideration. As suggested by Morse and Luther [92], there are not only thermodynamic but also kinetic prerequisites for the formation of different TE-hosts in sediments deposited under oxygen-deficient conditions. Faster water exchange reaction kinetics for Pb, Zn, and Cd than for  $\text{Fe}^{2+}$  explains why MeS phases (Me = Pb, Zn, Cd) precipitate faster and prior to pyrite, whereas Co and Ni, which have slower  $\text{H}_2\text{O}$  exchange kinetics than  $\text{Fe}^{2+}$ , are commonly incorporated into pyrite. Although  $\text{Cu}^{2+}$  has higher water exchange rates than  $\text{Fe}^{2+}$ , this element commonly shows intricate behaviour in sulphidic sediments because it exists in both +2 and +1 oxidation states. In suboxic environments, Cu can incorporate into pyrite as impurity, form other sulphides, or occur as complex compounds (chelates) in the sediment [44,92,107,114]. Indeed, Cu in the samples we studied does show the most complicated speciation: it resides in pyrite and marcasite, forms chalcopyrite and nukundamite, occurs as metallic copper or as impurity in (Au, Ag) alloys.

Mercury, with its water exchange rate higher than in Fe, was expected to form its own mineral prior to  $\text{FeS}_2$  formation [92]. On the other hand, Hg shows the strongest chloride complexation and highest hydrolysis constant, which should retard its reactivity with  $[\text{HS}^-]$  and allow incorporation of Hg into  $\text{FeS}_2$ . Previously, sequential extraction results for anoxic marine sediments led Huerta-Diaz and Morse [107] to infer that all Hg could reside in pyrite. We have not seen published evidence of Hg capability to form its own phases during diagenesis. Possibly, the discovery of cinnabar crystals in the Maykop Shales is the first find of this kind.

Unfortunately, we failed to find pyrite intergrown with other sulphides but  $\text{Ag}_2\text{S}$ , which would provide an explicit record of the crystallisation sequence. However, purification of pyrite crystals from most TE impurities we observed is evidence of conditions favourable for the growth of authigenic sulphides, as well as metallic species and alloys, both before and after the crystallisation of framboidal pyrite.

According to the criteria suggested by Large et al. [115], the Maykop sedimentary pyrites may be classified as diagenetic arsenian with refractory (dissolved) gold. Given that the pyrites contain no more than 0.06 ppm Au, the Oligocene-Miocene sediments of the Indol-Kuban Trough are unproductive [115]. Nevertheless, pyrite recrystallisation was accompanied by purification from the Au impurity and formation of free gold particles.

### 5.3. Degree of Anoxia/Oxygenation in Sediments: Mineralogical and Geochemical Constraints

The data on the authigenic mineral assemblages of the studied MMs can place more rigorous constraints on the degree of anoxia during the parent rocks deposition. The predominance of Fe(Mn)-carbonates over FeS<sub>2</sub> phases indicates transitional suboxic-to-anoxic depositional environments [48,94]. At significant inputs of highly reactive Fe (oxy)hydroxides into bottom sediments, the precipitation of Fe and/or Mn carbonates was mainly governed by active (unchelated) metals in the pore solutions whereas the crystallisation of sulphides was very likely limited by local concentrations of microbially-produced sulphidic sulphur. The environmental conditions during the precipitation of Fe(Mn) carbonates were weakly reducing but non-sulphidic, according to the classification in [46]. Oxygen depletion occurs in subbottom mud but sulphate reduction has not completed yet. Berner [116] estimated such conditions numerically as [O<sub>2</sub>] < 10<sup>-6</sup> mol/L and [H<sub>2</sub>S] < 10<sup>-6</sup> mol/L.

TE pyrite composition can be used as effective proxy for anoxia estimations [48,81], namely, Re, Se, Te with marked storages in the analysed pyrites, are proxy of environment oxygenation/reduction. According to the criteria of Parnell et al. [48], a Re/Mo ratio of about 0.006 (>0.005) estimated for the Andrusov Hill framboids characterises the host sediments as deposited in suboxic environments, whereas the lower Re/Mo ratio (<0.002) in the Tischenko Hill framboids indicates a more reducing environment. Other relative concentrations of redox sensitive elements such as Te/Se, Sb/Se and Tl/Se (Table 7) in pyrite framboids concordantly decrease from the highest values in the Andrusov Hill samples to the lowest ones in those from Tischenko Hill. This trend also reveals [48] the highest degree of pore water oxygenation in the former case and the most reducing depositional environment in the latter one, with intermediate characteristics for the Trubetskoy Hill sediments. The δ<sup>34</sup>S depletion of authigenic pyrite likewise supports its growth under weakly sulphidic conditions [42,46]. The δ<sup>34</sup>S decrease from the heaviest in the framboids from Andrusov Hill (δ<sup>34</sup>S = +8.9‰) to the lightest in the Tischenko Hill sample (+0.4‰ and -1.5‰ for framboids) (Figure 15) confirms that framboidal pyrite formed under restricted microbially-induced sulphate reduction, which was very low in the former case.

## 6. Conclusions

The obtained data on mineralogy, mineral chemistry, and TE compositions of both bulk rocks/fractions and separate minerals reveal three mineral assemblages in the mud volcanic ejecta from the Bulganak field. The three assemblages differ in origin and each bears evidence of the deposition environments of the parent mudrocks (Miocene Middle Maykop shales), which are currently extruded by mud volcanoes.

Clay minerals store a record of the provenance of material transported to the sedimentary basin and the maturity of the currently extruded sediments. High illite/smectite ratios in MMs that experienced diagenetic alteration at 80–100 °C are consistent with fluid generation temperatures (T<sub>Mg/Li</sub>) from 76 to 117 °C. The Bulganak MVs are fed from a mud reservoir located at a depth of 2.5–3.5 km, which corresponds to the depth of the lower Middle Maykop Formation in the north-eastern Kerch Peninsula. Ultrastable and non-resistant heavy mineral assemblages indicate the principal and subordinate provenance areas: the Ukrainian shield and the Greater Caucasus, respectively. High contents of kaolinite also support clastic inputs to the western termination of the Indol-Kuban Trough mostly from the southern Russian Platform.

The MMs from the Bulganak area are remarkable by diverse authigenic mineralogy: seven mineral species of carbonates, including complex Fe–Mg–Mn–(Ca) carbonates, eight species of sulphides, three metallic species (Cu, Au and Au–Ag alloy), quartz, glauconite, and apatite. The concordant changes of TE compositions and O, C, and S isotopic signatures in the authigenic carbonates and sulphides confirm their syngenetic origin. We checked several geochemical criteria which strongly indicate that the authigenic assemblages formed during early diagenesis under suboxic depositional conditions in a (SO<sub>4</sub>)<sup>2-</sup>-rich medium, at suppressed sulphate reduction and inhibited methanogenesis.

These conditions were favorable for complete  $\text{Mn}^{3(4)+}$  to  $\text{Mn}^{2+}$  reduction followed by partial reduction of  $\text{Fe}^{3+}$  to  $\text{Fe}^{2+}$ , and subsequent Fe(Mn)-rich carbonate precipitation before sulphate-reduction and Fe sulphide formation. The co-precipitation of predominant Fe(Mn)-rich carbonates with lesser amounts of TE-enriched Fe sulphides inferred for the Bulganak MMs is common to the settings of sufficient reactive iron supply and  $\text{Fe}^{3+}$  reduction at rates faster than sulphate reduction [101]. This highly TE loaded pyrite incorporates the same TE elements (Mo, As, Ni, Cu, Se, Re, Sb, Tl) as the Cenozoic oxygenated ocean [81]. During sediment maturation, earlier pyrite framboids recrystallise and loose TE, which then become stored as sulphides, metals or alloys. Thus the above physicochemical conditions, together with kinetic factors, are jointly responsible for the diverse authigenic mineralogy of the extruded mud masses.

We failed to find any solids produced by reactions of described authigenic minerals with very specific (Na-, Cl-, B-, and Li-rich) MV aqueous fluids. Possible reasons are: (1) low water/rock ratios and very low porosity of mud masses; (2) encapsulation of individual authigenic mineral grain in compact clayey coats; (3) short duration of water-rock interaction during MMs ascent and extrusion. The mineral-forming potential of MV aqueous fluids can fully realise only upon abrupt changes of physicochemical conditions when fluid are expelled to the surface. MV fluids can generate very specific mineral assemblages of salt crusts rapidly growing on the evaporation barrier.

**Supplementary Materials:** The following are available online at <http://www.mdpi.com/2075-163X/8/8/344/s1>, Table S1: The supplementary information details the LA-ICPMS analytical method for in situ  $\text{FeS}_2$  analysis.

**Author Contributions:** Project idea: E.S., S.K., O.K.; Mineralogy and petrography: E.S., S.K. and S.N.; Field work: E.S., S.K., S.N. and M.K.; EPMA analyses: E.N.; Writing: E.S., S.K., O.K., and S.N.; ICP-MS analysis and preconditioning of samples: O.K.; XRD analysis, and preconditioning of samples, and interpretation: P.K. and E.B.

**Funding:** This research was funded by the Russian Science Foundation, grant number 17-17-01056

**Acknowledgments:** The manuscript benefited much from the thoughtful review and valuable comments by anonymous reviewers. We kindly appreciate the fruitful scientific collaboration of our colleagues from the Department of Marine Geology and Sedimentary Ore Formation, NAS of the Ukraine (Kiev, Ukraine) and personally academician Ye.F. Shnyukov. We would like to thank V.S. Kamenetsky (School of Physical Sciences University of Tasmania, Hobart, Australia) and C. März (University of Leeds, UK) for constructive criticism of the initial manuscript version, valuable comments and their helpful suggestions. We further thank T. Perepelova as well as M. Khlestov (IGM, Novosibirsk) for their helpful advice to the present work. We kindly appreciate Ivan Belousov (ARC Centre of Excellence in Ore Deposits (CODES), University of Tasmania, Hobart, Australia) for the LA-ICPMS analyses of pyrite. The study was supported by the Russian Science Foundation, grant 17-17-01056.

**Conflicts of Interest:** The authors declare no conflict of interest.

## References

1. Rakhmanov, R.R. *Mud Volcanoes and Their Petroleum Potential*; Nedra: Moscow, Russia, 1987. (In Russian)
2. Kopf, A. Significance of mud volcanism. *Rev. Geophys.* **2002**, *40*, 1–52. [[CrossRef](#)]
3. Shnyukov, E.; Sheremetiev, V.; Maslakov, N.; Kutniy, V.; Gusakov, I.; Trofimov, V. *Mud Volcanoes of the Kerch-Taman Region*; GlavMedia Publishing House: Krasnodar, Russia, 2005. (In Russian)
4. Evans, R.J.; Davies, R.J.; Stewart, S.A. Internal structure and eruptive history of a kilometre-scale mud volcano system, South Caspian Sea. *Basin Res.* **2007**, *19*, 153–163. [[CrossRef](#)]
5. Alizadeh, A.A. *Geology of Azerbaijan, Oil and Gas, v. VII*; Nafta-Press: Baku, Azerbaijan, 2009. (In Russian)
6. Mazzini, A. Mud volcanism: Processes and implications. *Mar. Pet. Geol.* **2009**, *26*, 1677–1680. [[CrossRef](#)]
7. Dimitrov, L. Mud volcanoes as the most important pathways for degassing deeply buried sediments. *Earth Sci. Rev.* **2002**, *59*, 49–76. [[CrossRef](#)]
8. Planke, S.; Svensen, H.; Hovland, M.; Banks, D.A.; Jamtveit, B. Mud and fluid migration in active mud volcanoes in Azerbaijan. *Geo-Mar. Lett.* **2003**, *23*, 258–268. [[CrossRef](#)]
9. Martinelli, G.; Panahi, B. *Mud Volcanoes, Geodynamics and Seismicity*; Springer: Dordrecht, The Netherlands, 2005.
10. Deville, E.; Guerlais, S.H. Cyclic activity of mud volcanoes: Evidences from Trinidad (SE Caribbean). *Mar. Pet. Geol.* **2009**, *26*, 1681–1691. [[CrossRef](#)]
11. Bonini, M.; Mazzarini, F. Mud volcanoes as potential indicators of regional stress and pressurized layer depth. *Tectonophysics* **2010**, *494*, 32–47. [[CrossRef](#)]

12. Feyzullayev, A.A. Mud volcanoes in the South Caspian basin: Nature and estimated depth of its products. *Nat. Sci.* **2012**, *4*, 445–453. [[CrossRef](#)]
13. Bonini, M.; Tassi, F.; Feyzullayev, A.A.; Aliyev, C.S.; Capecchiacci, F.; Minissaleet, A. Deep gases discharged from mud volcanoes of Azerbaijan: New geochemical evidence. *Mar. Pet. Geol.* **2013**, *43*, 450–463. [[CrossRef](#)]
14. Chao, H.C.; You, C.F.; Liu, H.C.; Chung, H.C. The origin and migration of mud volcano fluids in Taiwan: Evidence from hydrogen, oxygen, and strontium isotopic compositions. *Geochim. Cosmochim. Acta* **2013**, *114*, 29–51. [[CrossRef](#)]
15. Li, N.; Huang, H.; Chen, D. Fluid sources and chemical processes inferred from geochemistry of pore fluids and sediments of mud volcanoes in the southern margin of the Junggar Basin, Xinjiang, northwestern China. *Appl. Geochem.* **2014**, *46*, 1–9. [[CrossRef](#)]
16. Oppo, D.; Capozzi, R.; Nigarov, A.; Esenov, P. Mud volcanism and fluid geochemistry in the Cheleken peninsula, western Turkmenistan. *Mar. Pet. Geol.* **2014**, *57*, 122–134. [[CrossRef](#)]
17. Kokh, S.N.; Sokol, E.V.; Dekterev, A.A.; Kokh, K.A.; Rashidov, T.M.; Tomilenko, A.A.; Bul'bak, T.A.; Khasaeva, A.; Guseinov, A. The 2011 Strong Fire Eruption of Shikhzarli Mud Volcano, Azerbaijan: A Case Study with Implications for Methane Flux Estimation. *Environ. Earth Sci.* **2017**, *76*, 701. [[CrossRef](#)]
18. Sokol, E.V.; Kokh, S.N.; Kozmenko, O.A.; Lavrushin, V.Y.; Kikvadze, O.A. Mud volcanoes as important pathway for trace elements input to the environment: Case study from the Kerch-Taman province, Northern Black Sea. In Proceedings of the SGEM 2018: 18th International Multidisciplinary Scientific GeoConference, Albena, Bulgaria, 2–8 July 2018; pp. 307–322.
19. Aliyev, A.A.; Guliyev, I.S.; Rakhmanov, R.R. *Catalogue of Mud Volcanoes Eruptions of Azerbaijan: 1810–2007*; Nafta-Press: Baku, Azerbaijan, 2009.
20. Sokol, E.; Novikov, I.; Zateeva, S.; Vapnik, Y.; Shagam, R.; Kozmenko, O. Combustion metamorphism in Nabi Musa dome: New implications for a mud volcanic origin of the Mottled Zone, Dead Sea area. *Basin Res.* **2010**, *22*, 414–438. [[CrossRef](#)]
21. Seryotkin, Y.V.; Sokol, E.V.; Kokh, S.N. Natural pseudowollastonite: Crystal structure, associated minerals, and geological context. *Lithos* **2012**, *133–135*, 75–90. [[CrossRef](#)]
22. Grapes, R.; Sokol, E.; Kokh, S.; Kozmenko, O.; Fishman, I. Petrogenesis of Na-rich paralava formed by methane flares associated with mud volcanism, Altyn-Emel National Park, Kazakhstan. *Contrib. Miner. Pet.* **2013**, *165*, 781–803. [[CrossRef](#)]
23. Bagirov, E.; Lerche, I. Flame hazards in the South Caspian Basin. *Energy Explor. Exploit.* **1998**, *16*, 373–397.
24. Jakubov, A.A.; Grigoryants, B.V.; Aliev, A.D.; Babazade, A.D.; Veliev, M.M.; Gadzhiev, Y.A.; Guseinzade, I.G.; Kabulova, A.Y.; Kastryulin, N.S.; Matanov, F.A.; et al. *Mud Volcanism in the USSR Territory and Its Relation with Petroleum Potential*; Elm: Baku, Russia, 1980. (In Russian)
25. Avdusin, P.P. *Mud Volcanoes of the Crimea-Caucasian Geological Province. A Petrographic Study*; Izd. AS USSR: Moscow, Russia, 1948. (In Russian)
26. Yassir, N.A. Mud Volcanoes and the Behaviour of Overpressured Clays and Silts. Ph.D. Thesis, University of London, London, UK, 1989.
27. Mazzini, A.; Etiope, G. Mud volcanism: An updated review. *Earth-Sci. Rev.* **2017**, *168*, 81–112. [[CrossRef](#)]
28. Dill, H.G.; Kaufhold, S. The Totumo mud volcano and its near-shore marine sedimentological setting (North Colombia)—From sedimentary volcanism to epithermal mineralization. *Sediment. Geol.* **2018**, *366*, 14–31. [[CrossRef](#)]
29. Aliev, A.A.; Lavrushin, V.Y.; Kokh, S.V.; Sokol, E.V.; Petrov, O.L. Isotopic composition of pyritic sulfur from the mud volcanic ejecta in Azerbaijan. *Lithol. Miner. Resour.* **2017**, *52*, 358–368. [[CrossRef](#)]
30. Aloisi, G.; Bouloubassi, I.; Heijs, S.; Pancost, R.D.; Pierre, C.; Sinninghe Damsté, J.S.; Gottschal, J.C.; Forney, L.J.; Rouchy, J.M. CH<sub>4</sub>-consuming microorganisms and the formation of carbonate crusts at cold seeps. *Earth Planet. Sci. Lett.* **2002**, *203*, 195–203. [[CrossRef](#)]
31. Gontharet, S.; Pierre, C.; Blanc-Valleron, M.M.; Rouchy, J.M.; Fouquet, Y.; Bayon, G.; Foucher, J.P.; Woodside, J.; Masclé, J. Nature and origin of diagenetic carbonate crusts and concretions from mud volcanoes and pockmarks of the Nile deep-sea fan (eastern Mediterranean Sea). *Deep-Sea Res. Part II* **2007**, *54*, 1292–1311. [[CrossRef](#)]
32. Merinero, P.R.; Lunar, H.R.; Martínez, F.J. Mechanisms of trace metal enrichment in submarine, methane-derived carbonate chimneys from the Gulf of Cadiz. *J. Geochem. Explor.* **2012**, *112*, 297–305. [[CrossRef](#)]

33. Wang, S.; Magalhães, V.H.; Pinheiro, L.M.; Liu, J.; Yan, W. Tracing the composition, fluid source and formation conditions of the methane-derived authigenic carbonates in the Gulf of Cadiz with rare earth elements and stable isotopes. *Mar. Pet. Geol.* **2015**, *68*, 192–205. [[CrossRef](#)]
34. Carvalho, L.; Monteiro, R.; Figueira, P.; Miei, C.; Almeida, J.; Pereira, E.; Magalhães, V.; Pinheiro, L.; Vale, C. Vertical distribution of major, minor and trace elements in sediments from mud volcanoes of the Gulf of Cadiz: Evidence of Cd, As and Ba fronts in upper layers. *Deep-Sea Res. Part I* **2018**, *131*, 133–143. [[CrossRef](#)]
35. Ershov, V.V.; Levin, B.V. New data on the material composition of mud volcano products on Kerch Peninsula. *Dokl. Earth Sci.* **2016**, *471*, 1149–1153. [[CrossRef](#)]
36. Inan, S.; Yalcin, M.N.; Guliev, I.S.; Kuliev, K.; Feizullayev, A.A. Deep petroleum occurrences in the lower Kura depression, south Caspian Basin, Azerbaijan: An organic geochemical and basin modelling study. *Mar. Pet. Geol.* **1997**, *14*, 731–762. [[CrossRef](#)]
37. Feyzullayev, A.A.; Guliyev, I.S.; Tagiyev, M.F. Source potential of the Mesozoic Cenozoic rocks in the South Caspian Basin and their role in forming the oil accumulations in the Lower Pliocene reservoirs. *Pet. Geosci.* **2001**, *7*, 409–417. [[CrossRef](#)]
38. Fowler, S.R.; Mildenhall, J.; Zalova, S.; Riley, G.; Elsley, G.; Desplanques, A.; Guliyev, F. Mud volcanoes and structural development on Shah Deniz. *J. Pet. Sci. Eng.* **2000**, *28*, 189–206. [[CrossRef](#)]
39. Smith-Rouch, L.S. Oligocene–Miocene Maykop/Diatom Total Petroleum System of the South Caspian Basin Province, Azerbaijan, Iran, and Turkmenistan. *U.S. Geol. Surv. Bull.* **2006**, *2201*, 1–27.
40. Luther, G.W.; Meyerson, A.L.; Krajewski, J.J.; Hires, R. Metal sulfides in estuarine sediments. *J. Sediment. Res.* **1980**, *50*, 1117–1120. [[CrossRef](#)]
41. Chow, N.; Morad, S.; Al-Aasm, I.S. Origin of authigenic Mn-Fe carbonates and pore-water evolution in marine sediments: Evidence from Cenozoic strata of the Arctic Ocean and Norwegian–Greenland Sea (ODP LEG 151). *J. Sediment. Res.* **2000**, *70*, 682–699. [[CrossRef](#)]
42. Rickard, D. *Sulfidic Sediments and Sedimentary Rocks*; Elsevier: Amsterdam, The Netherlands, 2012.
43. Fleurance, S.; Cuney, M.; Malartre, M.; Reyx, J. Origin of the extreme polymetallic enrichment (Cd, Cr, Mo, Ni, U, V, Zn) of the Late Cretaceous–Early Tertiary Belqa Group, central Jordan. *Palaeogeogr. Palaeoclimatol.* **2013**, *369*, 201–219. [[CrossRef](#)]
44. Gregory, D.D.; Large, R.R.; Halpin, J.A.; Lounejeva Baturina, E.; Lyons, T.W.; Wu, S.; Danyushevsky, L.; Sack, P.J.; Chappaz, A.; Maslennikov, V.V.; et al. Trace element content of sedimentary pyrite in black shales. *Econ. Geol.* **2015**, *110*, 1389–1410. [[CrossRef](#)]
45. Little, S.H.; Vance, D.; Lyons, T.W.; McManus, J. Controls on trace metal authigenic enrichment in reducing sediments: Insights from modern oxygen-deficient settings. *Am. J. Sci.* **2015**, *315*, 77–119. [[CrossRef](#)]
46. März, C.; Poulton, S.W.; Beckmann, B.; Kuster, K.; Wagner, T.; Kasten, S. Redox sensitivity of P cycling during black shale formation: Dynamics of sulfidic and anoxic, non-sulfidic bottom waters. *Geochim. Cosmochim. Acta* **2008**, *72*, 3703–3717. [[CrossRef](#)]
47. Sokol, E.V.; Kozmenko, O.A.; Khoury, H.N.; Kokh, S.N.; Novikova, S.A.; Nefedov, A.A.; Sokol, I.A.; Zaikin, P. Calcareous sediments of the Muwaqqar Chalk Marl Formation, Jordan: Mineralogical and geochemical evidences for Zn and Cd enrichment. *Gondwana Res.* **2017**, *46*, 204–226. [[CrossRef](#)]
48. Parnell, J.; Perez, M.; Armstrong, J.; Bullock, L.; Feldmann, J.; Boyce, A.J. Geochemistry and metallogeny of Neoproterozoic pyrite in oxic and anoxic sediments. *Geochem. Perspect. Lett.* **2018**, *7*, 12–16. [[CrossRef](#)]
49. Okay, A.I.; Şengör, A.M.C.; Görür, N. Kinematic history of the opening of the Black Sea and its effect on the surrounding regions. *Geology* **1994**, *22*, 267–270. [[CrossRef](#)]
50. Sidorenko, A.V. *Geology of USSR, v. VIII (Crimea)*; Nedra: Moscow, Russia, 1969. (In Russian)
51. Zonenshain, L.P.; Le Pichon, X. Deep basins of the Black Sea and Caspian Sea as remnants of Mesozoic back-arc basins. *Tectonophysics* **1986**, *123*, 181–240. [[CrossRef](#)]
52. Nedumov, R.I. Lithology, geochemistry, and paleogeography of Cenozoic deposits in the Caucasus foothills. *Litologiya i Poleznye Iskopaemye* **1994**, *1*, 69–77. (In Russian)
53. Lavrushin, V.Y.; Kopf, A.; Deyhle, A.; Stepanets, M.I. Formation of mud-volcanic fluids in Taman (Russia) and Kakhetia (Georgia): Evidence from boron isotopes. *Lithol. Miner. Resour.* **2003**, *38*, 120–153. [[CrossRef](#)]
54. Popov, S.V.; Rögl, F.; Rozanov, A.Y.; Steininger, F.F.; Shcherba, I.G.; Kováč, M. *Lithological–Paleogeographic Maps of Paratethys. 10 Maps Late Eocene to Pliocene. Scale: 1:5,000,000*; Courier Forschungsinstitut Senckenberg: Stuttgart, Germany, 2004.

55. Popov, S.V.; Antipov, M.P.; Zastrozhnov, A.S.; Kurina, E.E.; Pinchuk, T.N. Sea-level fluctuations on the northern shelf of the Eastern Paratethys in the Oligocene-Neogene. *Stratigr. Geol. Correl.* **2010**, *18*, 200–224. [[CrossRef](#)]
56. Kopf, A.; Deyhle, A.; Lavrushin, V.Y.; Polyak, B.G.; Gieskes, J.M.; Buachidze, G.I.; Wallmann, K.; Eisenhauer, A. Isotopic evidence (He, B, C) for deep fluid and mud mobilization from mud volcanoes in the Caucasus continental collision zone. *Int. J. Earth Sci. (Geol. Rundsch)* **2003**, *92*, 407–425. [[CrossRef](#)]
57. Meisner, A.; Krylov, O.; Nemcok, M. Development and structural architecture of the Eastern Black Sea. *Lead. Edge* **2009**, *28*, 1046–1055. [[CrossRef](#)]
58. Römer, M.; Sahling, H.; Pape, T.; Bahr, A.; Feseker, T.; Wintersteller, P.; Bohrmann, G. Geological control and magnitude of methane ebullition from a high-flux seep area in the Black Sea—the Kerch seep area. *Mar. Geol.* **2012**, *319–322*, 57–74. [[CrossRef](#)]
59. Kokh, S.N.; Shnyukov, Y.F.; Sokol, E.V.; Novikova, S.A.; Kozmenko, O.A.; Semenova, D.V.; Rybak, E.N. Heavy carbon travertine related to methane generation: A case study of the Big Tarkhan cold spring, Kerch Peninsula, Crimea. *Sediment. Geol.* **2015**, *325*, 26–40. [[CrossRef](#)]
60. Herbin, J.P.; Saint-Germès, M.; Maslakov, N.; Shnyukov, E.F.; Vially, R. Oil seeps from the “Boulganack” mud volcano in the Kerch Peninsula (Ukraine-Crimea), study of the mud and the gas: Inferences for the petroleum potential. *Oil Gas Sci. Technol.* **2008**, *63*, 609–628. [[CrossRef](#)]
61. Olenchenko, V.V.; Shnyukov, Y.F.; Gas'kova, O.L.; Kokh, S.N.; Sokol, E.V.; Bortnikova, S.B.; El'tsov, I.N. Explosion Dynamics of the Andrusov Mud Vent (Bulganak Mud Volcano Area, Kerch Peninsula, Russia). *Dokl. Earth Sci.* **2015**, *464*, 951–955. [[CrossRef](#)]
62. Nosovsky, M.F. The regional stratigraphic scale of the Maikopian deposits of the Crimea plain. *Geologicheskyy Zhurnal* **2003**, *3*, 137–145. (In Russian)
63. Seidov, A.G. *Lithology of the Maykop Formation in Azerbaijan*; Izd. Akademii Nauk Azerbaidzhanskoi SSR: Baku, Russia, 1962. (In Russian)
64. Lavrushin, V.Y.; Aidarkozhina, A.; Kikvadze, O.E.; Kokh, S.N. Geochemistry of mud volcanic fluids in the southern West-Kuban Basin: A case study with implication for source and mobilization depth reconstruction. In Proceedings of the XXII Conference on Groundwater in Siberia and Far East, Yakutsk, Russia, 22–26 June 2018; pp. 291–297. (In Russian)
65. Kharaka, Y.K.; Mariner, R.H. Chemical Geothermometers and Their Application to Formation Waters from Sedimentary Basins. In *Thermal History of Sedimentary Basins. Methods and Case Histories*; Naeser, N.D., McCulloh, T.H., Eds.; Springer: New York, NY, USA, 1989; pp. 99–117.
66. Naumenko, A.D.; Naumenko, M.A. Main patterns of high-potential reservoirs in the northeastern Black Sea. *Geologiya i Poleznye Iskopaemye Mirovogo Okeana* **2008**, *4*, 49–58. (In Russian)
67. Smyslov, A.A. *Geothermal Map: Map of the Crustal Heat Flow Regime in the USSR Territory. Scale 1:10,000,000*; Ministry of Geology: Moscow, Russia, 1977. (In Russian)
68. Kikvadze, O.E.; Lavrushin, V.Y.; Pokrovskii, B.G.; Polyak, B.G. Isotope and chemical composition of gases from mud volcanoes in the Taman Peninsula and problem of their genesis. *Lithol. Miner. Resour.* **2014**, *49*, 491–504. [[CrossRef](#)]
69. Shatsky, V.; Sitnikova, E.; Kozmenko, O.; Palessky, S.; Nikolaeva, I.; Zayachkovsky, A. Behavior of incompatible elements during ultrahigh-pressure metamorphism (by the example of rocks of the Kokchetav massif). *Russ. Geol. Geophys.* **2006**, *47*, 482–496.
70. Saryg-ool, B.Y.; Myagkaya, I.N.; Kirichenko, I.S.; Gustaytis, M.A.; Shuvaeva, O.V.; Zhmodik, S.M.; Lazareva, E.V. Redistribution of elements between wastes and organic-bearing material in the dispersion train of gold-bearing sulfide tailings: Part I. Geochemistry and mineralogy. *Sci. Total Environ.* **2017**, *581–582*, 460–471. [[CrossRef](#)] [[PubMed](#)]
71. Lavrent'ev, Y.G.; Korolyuk, V.N.; Usova, L.V.; Nigmatulina, E.N. Electron probe microanalysis of rock-forming minerals with a JXA-8100 electron probe microanalyzer. *Russ. Geol. Geophys.* **2015**, *56*, 1428–1436. [[CrossRef](#)]
72. Beckhoff, B.; Kanngießler, B.; Langhoff, N.; Wedell, R.; Wolff, H. *Handbook of Practical X-ray Fluorescence Analysis*; Springer: Berlin/Heidelberg, Germany, 2006.
73. Hubert, F.; Caner, L.; Meuner, A.; Ferrage, E. Unraveling complex <2 μm clay mineralogy from soils using X-ray diffraction profile modeling on particle-size sub-fractions: Implications for soil pedogenesis and reactivity. *Am. Mineral.* **2012**, *97*, 384–398. [[CrossRef](#)]

74. Guggenheim, S.; Bain, D.C.; Bergaya, F.; Brigatti, M.F.; Drits, V.A.; Eberl, D.D.; Formoso, M.L.L.; Galán, E.; Merriman, R.J.; Peacor, D.R.; et al. Report of the Association Internationale Pour L'Étude Des Argiles (AIPEA) Nomenclature Committee for 2001: Order, Disorder and Crystallinity in Phyllosilicates and the use of the "Crystallinity Index". *Clay Miner.* **2002**, *37*, 389–393. [[CrossRef](#)]
75. Taylor, S.M.; McLennan, S.M. *The Continental Crust: Its Composition and Evolution*; Blackwell Science: Oxford, UK, 1985.
76. Rudnick, R.L.; Gao, S. *The composition of the continental crust Treatise on Geochemistry—The Crust*; Rudnick, R.L., Holland, H.D., Turekian, K.K., Eds.; Elsevier: Oxford, UK, 2003; pp. 1–64.
77. Romanek, C.S.; Jiménez-López, C.; Navarro, A.R.; Sánchez-Román, M.; Sahai, N.; Coleman, M. Inorganic synthesis of Fe–Ca–Mg carbonates at low temperature. *Geochim. Cosmochim. Acta* **2009**, *73*, 5361–5376. [[CrossRef](#)]
78. Anovitz, L.M.; Essen, E.J. Phase equilibrium in the system CaCO<sub>3</sub>–MgCO<sub>3</sub>–FeCO<sub>3</sub>. *J. Petrol.* **1987**, *28*, 389–414. [[CrossRef](#)]
79. Bau, M.; Dulski, P. Distribution of yttrium and rare earth elements in the Penge and Kuruman iron-formations, Transvaal Supergroup, South Africa. *Precambrian Res.* **1996**, *79*, 37–55. [[CrossRef](#)]
80. Bolhar, R.; Kamber, B.S.; Moorbath, S.; Fedo, C.M.; Whitehouse, M.J. Characterisation of early Archaean chemical sediments by trace element signatures. *Earth Planet. Sci. Lett.* **2004**, *222*, 43–60. [[CrossRef](#)]
81. Large, R.R.; Halpin, J.A.; Danyushevsky, L.V.; Maslennikov, V.V.; Bull, S.W.; Long, J.A.; Gregory, D.D.; Lounejeva, E.; Lyons, T.W.; Sack, P.J.; et al. Trace element content of sedimentary pyrite as a new proxy for deep-time ocean–atmosphere evolution. *Earth Planet. Sci. Lett.* **2014**, *389*, 209–220. [[CrossRef](#)]
82. Cabral, A.R.; Radtke, M.; Munnik, F.; Lehmann, B.; Reinholz, U.; Riesemeier, H.; Tupinambá, M.; Kwitko-Ribeiro, R. Iodine in alluvial platinum–palladium nuggets: Evidence for biogenic precious-metal fixation. *Chem. Geol.* **2011**, *281*, 125–132. [[CrossRef](#)]
83. Meisel, T.; Horan, M.F. Analytical methods for the highly siderophile elements. *Rev. Mineral. Geochem.* **2016**, *81*, 89–105. [[CrossRef](#)]
84. Hagvall, K.; Persson, P.; Karlsson, T. Spectroscopic characterization of the coordination chemistry and hydrolysis of gallium(III) in the presence of aquatic organic matter. *Geochim. Cosmochim. Acta* **2014**, *146*, 76–89. [[CrossRef](#)]
85. Rice, C.M.; Atkin, D.; Bowels, J.F.W.; Criddle, A.J. Nukundamite, a new mineral, and idaite. *Mineral. Mag.* **1979**, *43*, 193–200. [[CrossRef](#)]
86. Hatert, F. Transformation sequences of copper sulfides at Vielsalm, Stavelot Massif, Belgium. *Can. Mineral.* **2005**, *43*, 623–635. [[CrossRef](#)]
87. Hámor-Vido, M.; Viczián, I. Vitrinite reflectance and smectite content of Mixed-layer illite/smectites in Neogene Sequences of the Pannonian Basin, Hungary. *Acta Geol. Hung.* **1993**, *36/2*, 197–209.
88. Stefanov, Y. Illite/smectite diagenesis and thermal evolution of Lower Cretaceous–Paleogene successions in the Dolna Kamchiya Depression, Eastern Bulgaria. *Geol. Balc.* **2018**, *47*, 3–21.
89. Huang, W.-L.; Bassett, W.A.; Wu, T.-C. Dehydration and hydration of montmorillonite at elevated temperatures and pressures monitored using synchrotron radiation. *Am. Mineral.* **1994**, *79*, 683–691.
90. Huggett, J. Low-temperature illitization of smectite in the late Eocene and early Oligocene of the Isle of Wight (Hampshire basin), UK. *Am. Mineral.* **2005**, *90*, 1192–1202. [[CrossRef](#)]
91. Hall, P.L.; Astill, D.M.; McConnell, J.D.C. Thermodynamic and structural aspects of the dehydration of smectites in sedimentary rocks. *Clay Miner.* **1986**, *21*, 633–648. [[CrossRef](#)]
92. Morse, J.W.; Luther, G.W. Chemical influences on trace metal-sulfide interactions in anoxic sediments. *Geochim. Cosmochim. Acta* **1999**, *63*, 3373–3378. [[CrossRef](#)]
93. Rue, E.L.; Smith, G.J.; Cutter, G.A.; Bruland, K.W. The response of trace element redox couples to suboxic conditions in the water column. *Deep-Sea Res.* **1997**, *44*, 113–134. [[CrossRef](#)]
94. Cutter, G.A.; Moffett, J.G.; Nielsdóttir, M.C.; Sanial, V. Multiple oxidation state trace elements in suboxic waters off Peru: In situ redox processes and advective/diffusive horizontal transport. *Mar. Chem.* **2018**, *201*, 77–89. [[CrossRef](#)]
95. Mucci, A. Manganese uptake during calcite precipitation from seawater: Conditions leading to formation of pseudokutnahorite. *Geochim. Cosmochim. Acta* **1988**, *52*, 1859–1868. [[CrossRef](#)]
96. Böttcher, M.E. Manganese (II) partitioning during experimental precipitation of rhodochrosite–calcite solid solutions from aqueous solutions. *Mar. Chem.* **1998**, *62*, 287–297. [[CrossRef](#)]

97. Millero, F.J.; Feistel, R.; Wright, D.G.; McDougall, T.J. The composition of Standard Seawater and the definition of the Reference-Composition Salinity Scale. *Deep-Sea Res.* **2008**, *55*, 50–72. [[CrossRef](#)]
98. Zachara, J.M.; Cowan, C.E.; Resch, C.T. Sorption of divalent metals on calcite. *Geochim. Cosmochim. Acta* **1991**, *55*, 1549–1562. [[CrossRef](#)]
99. Alwan, K.A.; Williams, P.A. Mineral formation from aqueous solution. Part I. The deposition of hydrozincite,  $Zn_5(OH)_6(CO_3)_2$ , from natural waters. *Transit. Met. Chem.* **1979**, *4*, 128–132. [[CrossRef](#)]
100. Abanda, P.A.; Hannigan, R. Effect of diagenesis on trace element partitioning in shales. *Chem. Geol.* **2006**, *230*, 42–59. [[CrossRef](#)]
101. Rajan, S.; Mackenzie, F.T.; Glenn, C.R. A thermodynamic model for water column precipitation of siderite in the Plio-Pleistocene Black Sea. *Am. J. Sci.* **1996**, *296*, 506–548. [[CrossRef](#)]
102. Campbell, K.A. Hydrocarbon seep and hydrothermal vent paleoenvironments and paleontology: Past developments and future research directions. *Palaeogeogr. Palaeoclimatol.* **2006**, *232*, 362–407. [[CrossRef](#)]
103. Roberts, H.H.; Feng, D.; Joye, S.B. Cold-seep carbonates of the middle and lower continental slope, northern Gulf of Mexico. *Deep-Sea Res. Part II* **2010**, *57*, 2040–2054. [[CrossRef](#)]
104. Matsumoto, R.; Ryu, B.J.; Lee, S.R.; Lin, S.; Wu, S.; Sain, K.; Pecher, I.; Riedel, M. Occurrence and exploration of gas hydrate in the marginal seas and continental margin of the Asia and Oceania region. *Mar. Pet. Geol.* **2011**, *28*, 1751–1767. [[CrossRef](#)]
105. Bruland, K.W.; Lohan, M.C. Controls of trace metals in seawater. In *Treatise on Geochemistry*; Elsevier: Amsterdam, The Netherlands, 2003; Volume 6, pp. 23–47.
106. Tribouillard, N.; Algeo, T.J.; Lyons, T.; Riboulleau, A. Trace metals as paleoredox and paleoproductivity proxies: An update. *Chem. Geol.* **2006**, *232*, 12–32. [[CrossRef](#)]
107. Huerta-Diaz, M.A.; Morse, J.W. Pyritization of trace metals in anoxic marine sediments. *Geochim. Cosmochim. Acta* **1992**, *56*, 2681–2702. [[CrossRef](#)]
108. Janssen, D.J.; Conway, T.M.; John, S.G.; Christian, J.R.; Kramer, D.I.; Pedersen, T.F.; Cullen, J.T. Undocumented water column sink for cadmium in open ocean oxygen-deficient zones. *Proc. Natl. Acad. Sci. USA* **2014**, *111*, 6888–6893. [[CrossRef](#)] [[PubMed](#)]
109. Awid-Pascual, R.; Kamenetsky, V.S.; Goemann, K.; Allen, N.; Noble, T.; Lottermoser, B.G.; Rodemann, T. The evolution of authigenic Zn–Pb–Fe-bearing phases in the Grieves Siding peat, western Tasmania. *Contrib. Mineral. Petrol.* **2015**, *170*, 17. [[CrossRef](#)]
110. Lane, T.W.; Morel, F.M. A biological function for cadmium in marine diatoms. *Proc. Natl. Acad. Sci. USA* **2000**, *97*, 4627–4631. [[CrossRef](#)] [[PubMed](#)]
111. Morel, F.M.M. The oceanic cadmium cycle: Biological mistake or utilization? *Proc. Natl. Acad. Sci. USA* **2013**, *110*, E1877. [[CrossRef](#)] [[PubMed](#)]
112. Mederer, J.; Moritz, R.; Zohrabyan, S.; Vardanyan, A.; Melkonyan, R.; Ulianov, A. Base and precious metal mineralization in Middle Jurassic rocks of the Lesser Caucasus: A review of geology and metallogeny and new data from the Kapan, Alaverdi and Mehmana districts. *Ore Geol. Rev.* **2014**, *58*, 185–207. [[CrossRef](#)]
113. Varentsov, I.M. *Manganese Ores of SuperGene Zone: Geochemistry of Formation*; Springer: Berlin, Germany, 1996.
114. Berner, Z.A.; Puchelt, H.; Nöltner, T.; Kramar, U. Pyrite geochemistry in the Toarcian Posidonia Shale of southwest Germany: Evidence for contrasting trace-element patterns of diagenetic and syngenetic pyrites. *Sedimentology* **2013**, *60*, 548–573. [[CrossRef](#)]
115. Large, R.R.; Bull, S.W.; Maslennikov, V.V. A carbonaceous sedimentary source-rock model for carlin-type and orogenic gold deposits. *Econ. Geol.* **2011**, *106*, 331–358. [[CrossRef](#)]
116. Berner, R.A. A new geochemical classification of sedimentary environments. *J. Sediment. Res.* **1981**, *51*, 359–365. [[CrossRef](#)]

